AD-A048 813

CALIFORNIA RESEARCH AND TECHNOLOGY INC WOODLAND HILLS   F/G 19/1
PARAMETRIC STUDY OF THE EFFECTS OF TARGET PROPERTIES, PROJECTIL--ETC(U)
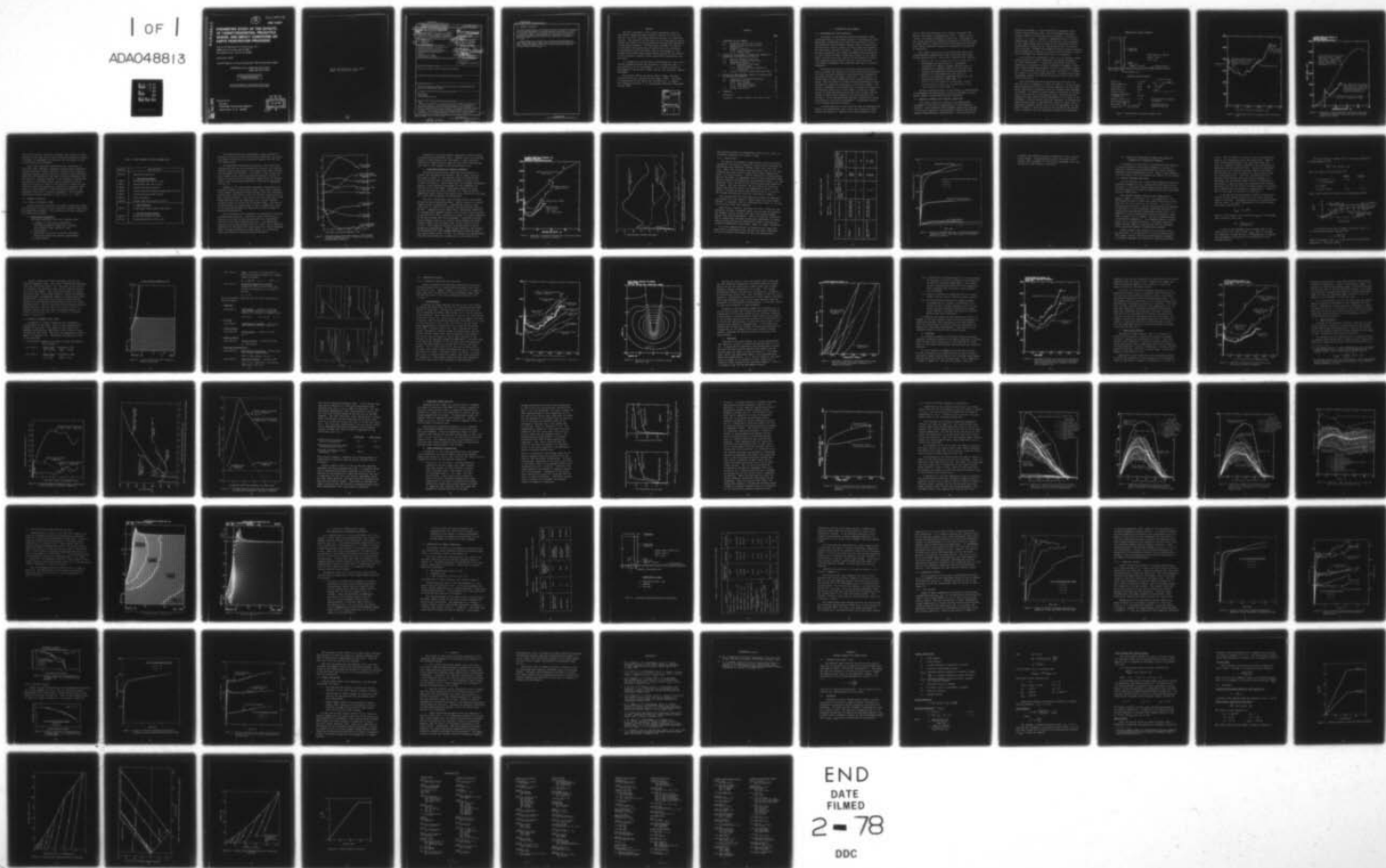NOV 76   M H WAGNER, C C FULTON   DNA001-75-C-0147
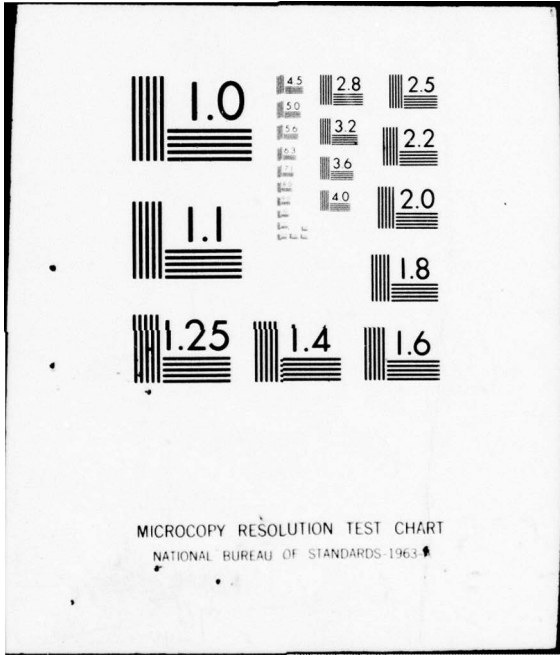UNCLASSIFIED   CRT-2080-3   DNA-4160T   NL

1 OF 1
ADA048813

END
DATE
FILMED
2-78
DDC

MICROCOPY RESOLUTION TEST CHART

NATIONAL BUREAU OF STANDARDS-1963

(12)

DNA 4160T

PARAMETRIC STUDY OF THE EFFECTS OF TARGET PROPERTIES, PROJECTILE DESIGN, AND IMPACT CONDITIONS ON EARTH PENETRATION PROCESSES

California Research & Technology, Inc.

6269 Variel Avenue, Suite 200

Woodland Hills, California 91364

November 1976

Topical Report for Period December 1974—December 1975

CONTRACT Nos. DNA 001-75-C-0147
DNA 001-76-C-0157

Prepared for

Director

DEFENSE NUCLEAR AGENCY

Washington, D. C. 20305

D D C

JAN 19 1978

B

Destroy this report when it is no longer
needed. Do not return to sender.

REPORT DOCUMENTATION PAGE	READ INSTRUCTIONS BEFORE COMPLETING FORM

1. REPORT NUMBER	2. GOVT ACCESSION NO.	3. RECIPIENT'S CATALOG NUMBER
DNA 4160T	AD-E300 076	

4. TITLE (and Subtitle)	5. TYPE OF REPORT & PERIOD COVERED
PARAMETRIC STUDY OF THE EFFECTS OF TARGET PROPERTIES, PROJECTILE DESIGN, AND IMPACT CONDITIONS ON EARTH PENETRATION PROCESSES.	Topical Report, Dec 74—Dec 75,
	6. PERFORMING ORG. REPORT NUMBER
	CRT-2080-3

7. AUTHOR(s)	8. CONTRACT OR GRANT NUMBER(s)
M. H. Wagner, C. C. Fulton, K. N. Kreyenhagen	DNA 001-75-C-0147, and DNA 001-76-C-0157

9. PERFORMING ORGANIZATION NAME AND ADDRESS	10. PROGRAM ELEMENT, PROJECT, TASK AREA & WORK UNIT NUMBERS
California Research & Technology, Inc. 6269 Variel Avenue, Suite 200 Woodland Hills, California 91364	NWED Subtask Y99QAXSB048-01

11. CONTROLLING OFFICE NAME AND ADDRESS	12. REPORT DATE
Director Defense Nuclear Agency Washington, D.C. 20305	Nov 76
	13. NUMBER OF PAGES
	85 p.

14. MONITORING AGENCY NAME & ADDRESS(if different from Controlling Office)	15. SECURITY CLASS. (of this report)
	UNCLASSIFIED
	15a. DECLASSIFICATION/DOWNGRADING SCHEDULE

16. DISTRIBUTION STATEMENT (of this Report)

Approved for public release; distribution unlimited.

17. DISTRIBUTION STATEMENT (of the abstract entered in Block 20, if different from Report)

18. SUPPLEMENTARY NOTES

This work sponsored by the Defense Nuclear Agency under RDT&E RMSS Code B344075464 Y99QAXSB04801 H2590D.

19. KEY WORDS (Continue on reverse side if necessary and identify by block number)

Penetration
Terradynamics
Finite-Difference Codes

20. ABSTRACT (Continue on reverse side if necessary and identify by block number)

There are a number of projectile and target parameters involved in the penetration dynamics of earth penetrating vehicles. The sensitivity of penetration processes to some of these parameters has been examined in a series of finite-difference code solutions. The spatial resolution required to obtain accurate code solutions of penetration dynamics has also been considered. The calculated penetration dynamics were not overly sensitive to variations in the target properties; the local shear strength and

DD FORM 1473 EDITION OF 1 NOV 65 IS OBSOLETE

391 223

20.   ABSTRACT (Continued)

frictional characteristics of the material acting on the penetrator appeared
to be the most important of the target parameters considered. A portion
of the study was devoted to consideration of the impact conditions and
the penetrator design. These variables were generally more important to
penetration dynamics than variations of the constitutive properties of
the target.

These findings are favorable to the technology and development of
earth penetrating weapons, since target property uncertainties are inevi-
table. Design and impact parameters, on the other hand, can generally
be specified and controlled.

PREFACE

The work described in this report constitutes part of
the efforts authorized under Contracts DNA 001-75-C-0147 and
DNA 001-76-C-0157, concerning numerical analyses of earth pene-
trators. The objective of this part of the investigation was to
examine the effects of various numerical and physical parameters
on penetration dynamics. Related tasks included (1) analyses
of the impact and penetration of projectiles into rock media,
in conjunction with field events and (2) development of a de-
coupled finite-difference/finite-element method for the analysis
of the structural response within projectiles penetrating into
the earth.

M. H. Wagner was the principal investigator for this project.
General program guidance and assistance in technical analysis
was provided by K. N. Kreyenhagen. C. C. Fulton assisted in
development of the material models and was the principal computer
programmer.

The Project Officer was Major Todd D. Stong, Strategic
Structures Division, Defense Nuclear Agency (DNA). Assistance
in coordination of the effort was provided by P. F. Hadala,
Soil Dynamics Division, U. S. Army Engineer Waterways Experiment
Station (WES).

CONTENTS

I. INTRODUCTION AND SUMMARY

1.1 BACKGROUND AND TASK OBJECTIVES

In support of the DNA Earth Penetrating Weapon (EPW) technology project, California Research & Technology has been developing, validating, and using "first-principle" finite-difference and finite-element computer codes for predicting and analyzing critical aspects of earth penetration dynamics and penetrator structural response. Such code solutions can provide information, not readily obtainable from experiments or other analytical means, about the stresses in the target media, stresses and forces applied to the penetrator surface (and resulting decelerations), and the stress and shock environments throughout the penetrator body and its internal components.

The primary objective of the task reported herein has been to examine the sensitivity of earth penetration processes to several physical parameters describing target properties, penetrator design, and impact conditions. Consideration of broad ranges of these parameters may be required during the design and evaluation of an EPW; increased knowledge of their influence on penetrator performance is therefore needed. For example, knowledge of the sensitivity of penetration processes to different properties of earth media is needed to enable design of earth penetrators which will work reliably against targets in media whose properties are both uncertain and variable. To the maximum extent possible, penetrators should be designed so that their performance is reasonably insensitive to target property variables.

A second objective of this task has been to determine the effects of computational zone size on the accuracy of earth penetration analyses. Regions where steep gradients occur,

3

such as near the penetrator nose, require reasonably fine spatial resolution by computational zones. Computer costs, however, are sharply dependent on zone size. Knowledge of the zoning required for adequate resolution in different types of target media is needed to guide future numerical solutions where several numerical analyses of alternative designs may be called for.

This report is one of a series which have been or are being published regarding CRT tasks in the DNA Earth Penetrating Weapon project. These other reported tasks include:

o Analysis of a soil penetration test at DRES (Ref. 1)
o Development and application of a decoupled technique for internal response analysis (Ref. 2)
o Formulation of improved models for treating rock fracture and comminution during penetration, and analysis of rock penetration test (Ref. 3)
o Analysis of alternative prototype designs for the Shallow Burst Munition (SBM) (Ref. 4)
o Analysis of the loading on a penetrator surface, and structural response of the penetrator, for a reverse ballistic test (Ref. 5)

Current continuing effort on the project is concentrating on development and application of analysis methods for asymmetric impacts (yawed and/or oblique incidence).

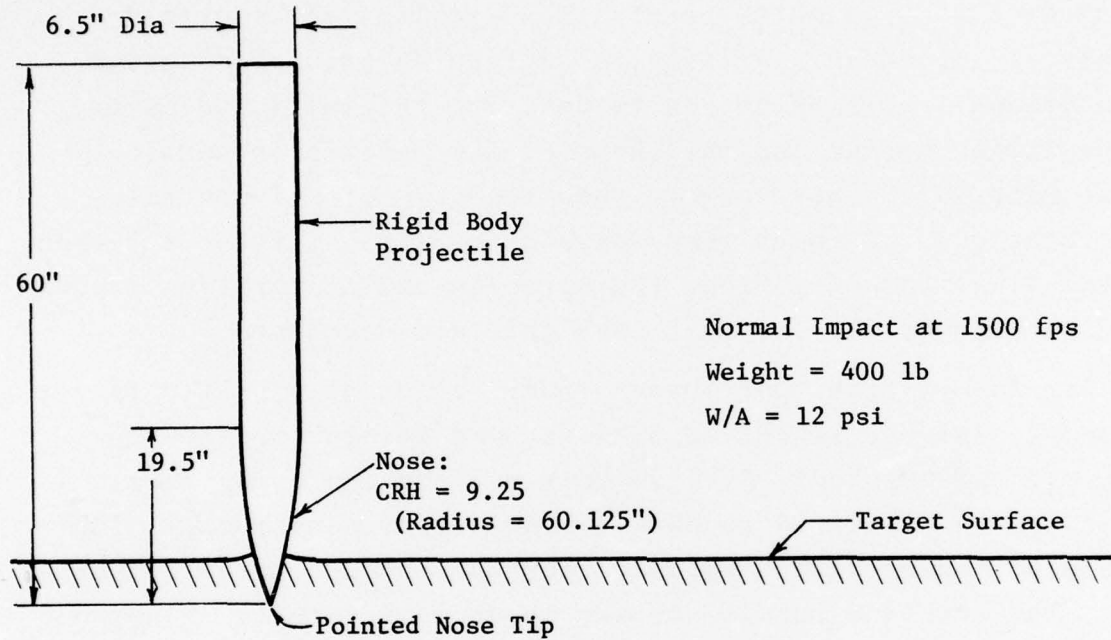1.2 TECHNICAL APPROACH AND BASELINE CONDITIONS

This task is based on a series of two-dimensional, axisymmetric solutions of penetrations of rigid body projectiles. Such solutions yield complete space-time histories of the forces exerted on the penetrator surface, and the consequent rigid-penetrator decelerations. The solutions were

4

obtained with WAVE-L, a finite-difference Lagrangian hydro-dynamic-elastic-plastic code. Prior development and application of WAVE-L to earth penetration problems is described in Refs. 1, 3, and 6. Briefly, a Lagrangian grid of discrete computational cells is set up to describe the initial geometry of the target medium and the shape of the penetrator surface. Target material properties are specified by sets of constitutive relations. Through time-stepped solution of these relations and the equations of motion, the stresses and distortions experienced throughout the computational grid are developed.

For the physical parameters study, a set of baseline target medium properties, impact conditions, and design parameters was first established. A rigid-body penetration using these conditions was analyzed to obtain standard, or benchmark, information about penetration dynamics for use in subsequent comparisons. The baseline conditions are shown in Figure 1. Sandstone was chosen as the basic target material. The penetrator design corresponds closely with the DNA projectile used in recent full-scale field tests[7].

The calculated projectile deceleration history for the baseline case in sandstone is shown in Figure 2. Forces on most earth penetrators build up as the nose advances into the target media, approaching a maximum as the nose becomes fully embedded, or "wetted". To enable a larger number of solutions to be made within the resources of the present study, the solutions were started with the nosetip already embedded to 5-in. depth in the sandstone. After an initial spurious transient, an acceleration ramp develops, which is qualitatively similar to those seen in penetrator problems started with no initial embedment, as indicated in Figure 3 (here the axial force instead of the deceleration is plotted since the penetrator weights were different).

5

PENETRATOR AND IMPACT CONDITIONS

6.5" Dia

Rigid Body
Projectile

60"

19.5"

Normal Impact at 1500 fps

Weight = 400 lb

W/A = 12 psi

Nose:
CRH = 9.25
(Radius = 60.125")

Target Surface

Pointed Nose Tip

SANDSTONE TARGET PROPERTIES

Density, ρ_o	2.0 g/cm^3
Young's modulus, E_o	72 kb
Bulk modulus, K_o	40 kb
Shear modulus, G_o	30 kb
Poisson's ratio, ν	0.2
Unconfined compressive strength,	0.41 kb
"Cohesion ($\sqrt{J_2'}$)", k_1	0.1 kb
Mohr-Coulomb slope, k_2	1
Mises limit ($\sqrt{J_2'}$), k_3	3 kb

Friction rule: $\tau = 0.15\sqrt{J_2'} (\sigma_n)$

$\sqrt{J_2'}$

Yield Surface

k_3

k_2

k_1

P
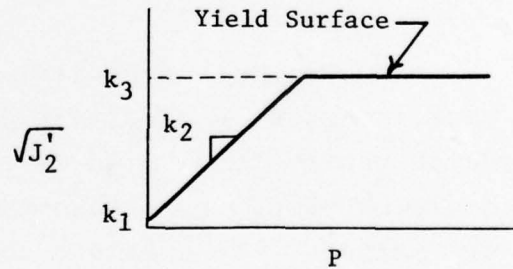
Fractured material degrades
in strength

Associated flow rule
(exhibits dilatancy)

Figure 1.   Baseline Case for Physical Parameter Study

6
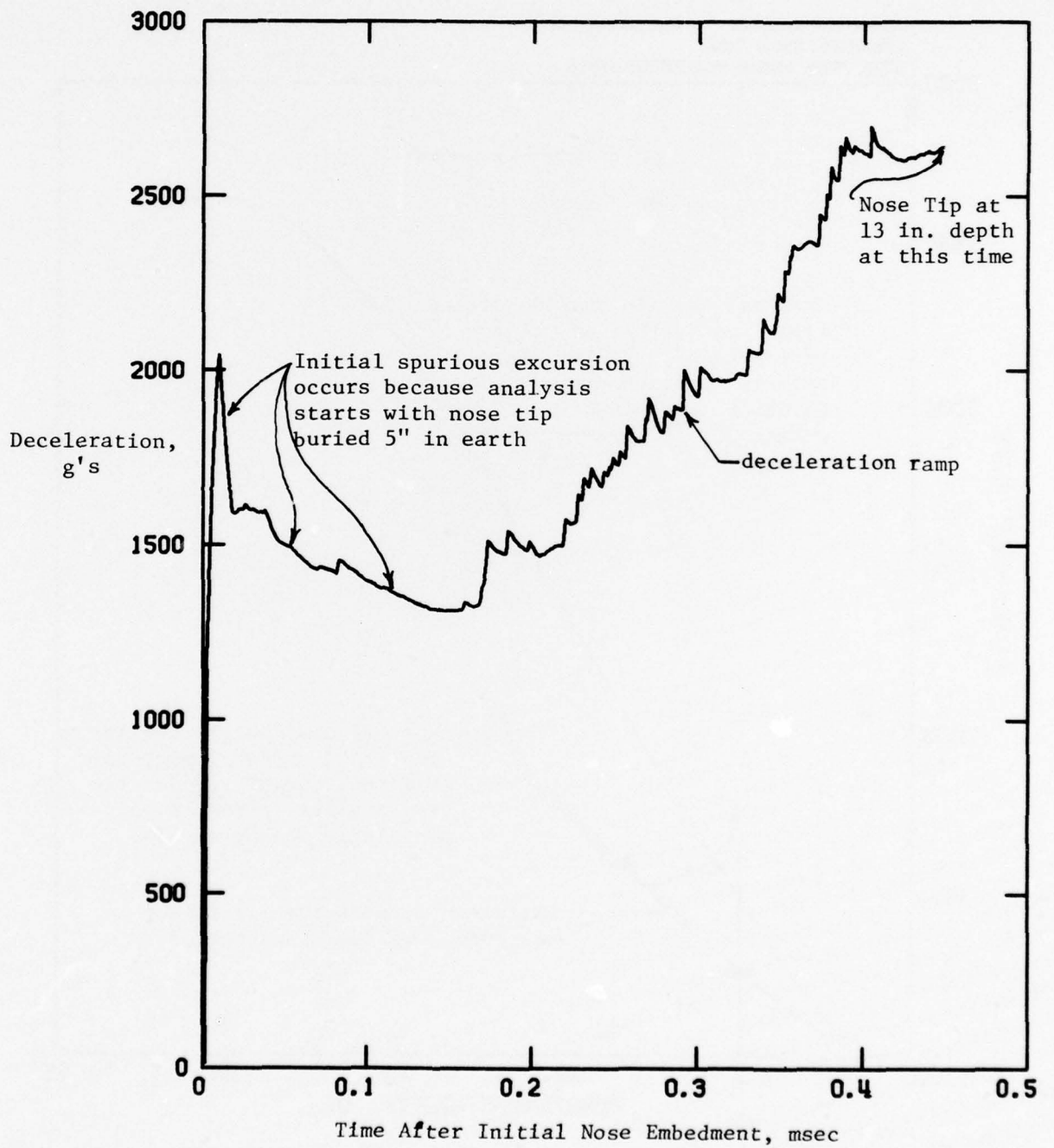
Figure 2. Deceleration History for Baseline Pointed Projectile Case

From calculation of 1500 ft/sec impact on surface of welded tuff target[3]. Projectile same as for parametric study baseline case except weight=517 lb.

From calculation of baseline case, 1500 ft/sec impact into sandstone target, projectile tip initially buried 5 in., projectile weight=400 lb.

Estimated force curve for impact on *surface* of sandstone target

Figure 3. Comparison of Deceleration Force Histories between Impact on Surface of Target and Impact with Nose Tip Initially Buried to 5-in. Depth.

8

Thus, if the initial transient is ignored, the results of calculations of this type can be used to show the qualitative effects of changes in independent variables on the resistance to penetration during nose embedment.

Since just rigid body penetrations were considered in this task, only "external" parameters (target media properties, external penetrator shape, and impact velocity) were examined. Internal response, and the effects of internal design parameters (materials and thicknesses and shock isolation techniques) were not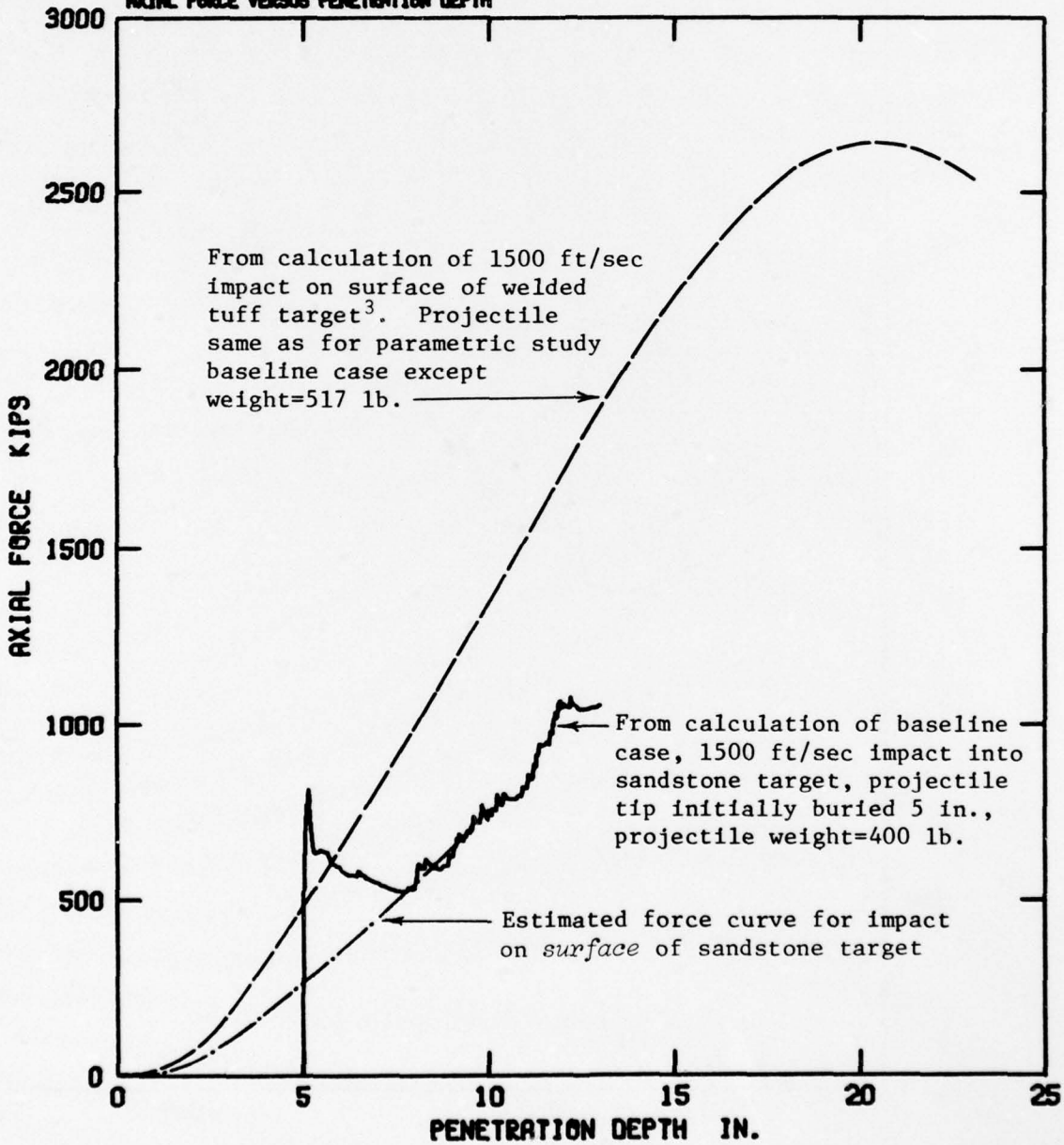 involved. Separate analyses of the response of penetrators, considered as deformable bodies, can be obtained using the space-time history of forces on the penetrator surface (as generated by rigid-body penetration solutions) as boundary conditions for finite-element or finite-difference models of the penetrator body and its internal components. This decoupled penetration-response approach is used in Res. 2, 5, and 8.

1.3 SUMMARY OF RESULTS

1.3.1 Physical Parameter Study

Eleven penetration solutions were made to determine effects of *independent* variations in basic physical variables upon rigid body penetration dynamics. The conditions for these solutions are summarized in Table 1.

a. Target Media Parameters
The target properties which were examined were:

o strength or yield surface parameters, including unconfined compressive strength, yield surface slope, and Mises limit
o bulk modulus
o coefficient of friction along the interface between the projectile and the target medium
o initial density

9

TABLE 1. CASES CONSIDERED IN PHYSICAL PARAMETER STUDY

Case No.	Case Description
2080-32C	Baseline case (see Fig. 1)
	a. Target Media Parameters
2080-60	Decrease Mises limit 50% (to 1.5 kb)
2080-61	Increase Mises limit 100% (to 6 kb)
2080-62	Decrease yield surface slope 50%
2080-65	Increase unconfined compressive strength 100% (to .82 kb)
2080-70	Increase bulk modulus 100% (to 80 kb)
2080-82	Delete all friction
2080-100	Increase target density 100% (to 4 gm/cm^3)
	b. Impact Parameters
2080-110	Increase impact velocity 100% (to 3000 ft/sec)
	c. Penetrator Design Parameters
2080-120	Decrease nose sharpness (to CRH=6)
2080-122	Increase penetrator dia ~50% (to 9 in.)

The changes which were considered in these properties (typically to half or twice the baseline condition) are within the range of variations which would be expected for EPW soft rock target media.

The penetrator deceleration histories, stress and force loading distributions on the penetrator surfaces, and profiles of peak stresses experienced in the target media were obtained from the numerical solutions. The effects of the target property changes on the overall penetration dynamics are seen in Figure 4, which shows the percentage change (from the baseline case) in the time-averaged penetrator deceleration $\left(\dfrac{V_o - V(t)}{t}\right)$ vs time (t).

Changes in the yield surface parameters (unconfined compressive strength, yield surface slope, Mises limit) produced 5-45% changes in penetrator deceleration, with those parameters defining the yield surface in the low kilobar regime having the more sensitive effects. This relects the fact that most of the target material near the penetrator nose is under maximum pressures which are within the low kilobar range. The effects of bulk modulus are interesting, in that a substantial change in the load-unload hydrostat caused only a modest change in penetrator deceleration.

The frictionless case confirmed the importance of friction in penetration processes. Relatively small coefficients of friction can result in drag forces which are a significant fraction of the total decelerating force. The appropriate friction rule, given the high velocity, stress, and temperature conditions at the penetrator-target interface, and the degraded state of target properties in that region, is a continuing major uncertainty in earth penetration mechanics.
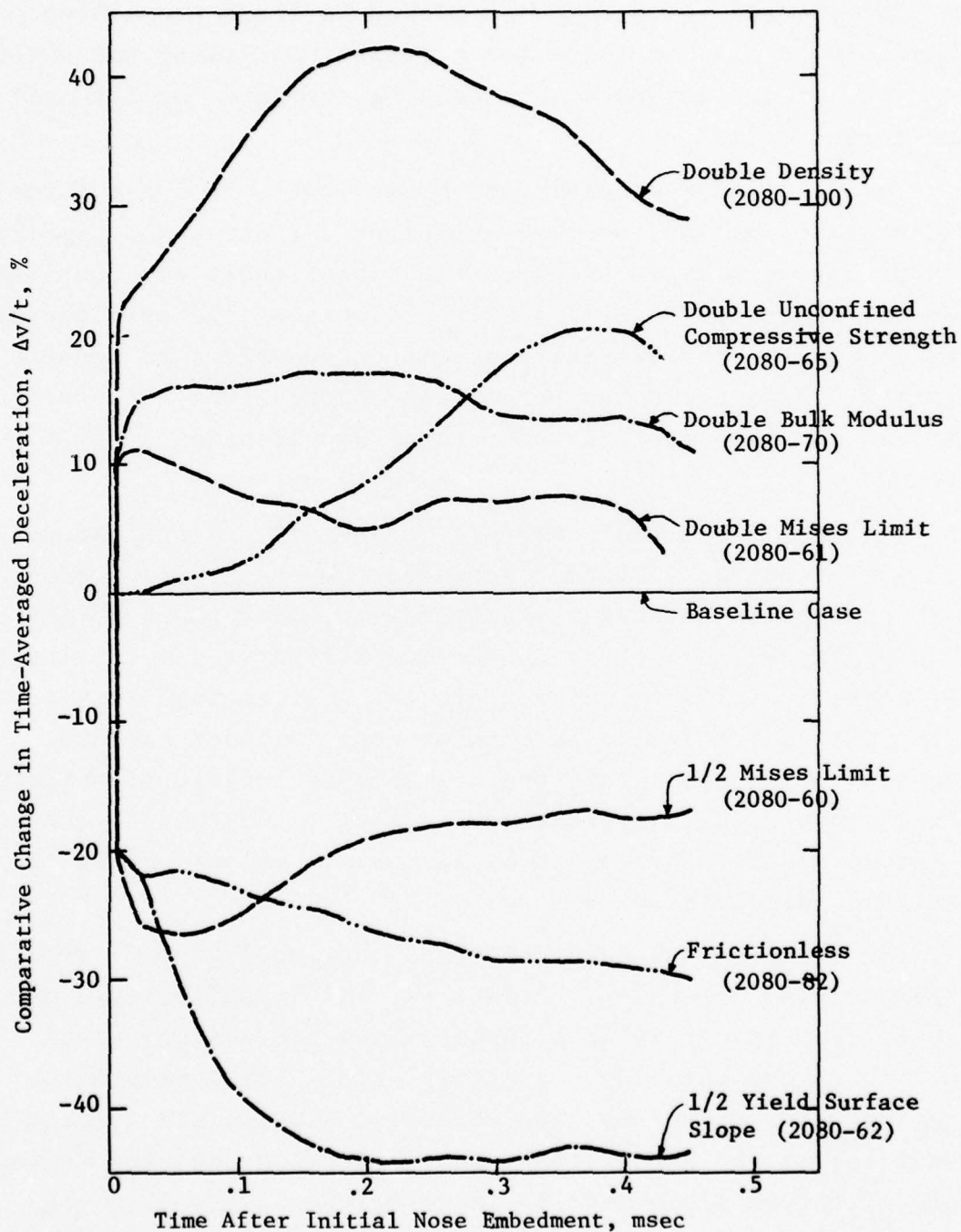
Figure 4. Percentage Change (from Baseline Case) in Time-Averaged
Penetrator Deceleration, Δv/t, vs Time Due to Variations
of Target Media Parameters.

12

Doubling of the target density produced a 30-40% increase in penetrator deceleration levels. However, this is an extreme change in target density for rock media. A more realistic variation in target density might be ±25%, which would presumably lead to ±10% changes in the deceleration level.

b. Penetrator Design and Impact Parameters

Penetrator decelerations resulting from variations in vehicle nose sharpness and diameter, and in impact velocity, are shown in Figure 5. The percent change in deceleration from the baseline case vs penetration depth for these cases is shown in Figure 6. These comparisons are somewhat misleading, however, since different percentages of nose embedment are involved at the same depth. Additional comparisons using scaling relations are given in Section 2.3. More definitive comparisons would require carrying out each solution to the point of a clear peak or plateau in deceleration.

From this limited data, the following effects were noted during the early penetration phase. Impact velocity is clearly a major factor in penetration: doubling the velocity from 1500 ft/sec to 3000 ft/sec increases the deceleration level by 60-130%. Changing the nose shape from a sharp ogive (CRH=9.25) to a medium ogive (CRH=6) results in an initially sharp increase in deceleration (~60%), followed by a decay to a small difference as the nose becomes more fully embedded. Increasing the penetrator diameter from 6.5 to 9 inches while holding the weight constant reduces the sectional load, or W/A, from 12 psi to 6.3 psi. This causes an increase in deceleration of 20-40% during early penetration. From scaling relations, the increase in deceleration for fully engaged penetrators would be inversely proportional to W/A, or 92%. If, however, the deceleration histories are plotted on a scaled basis, (see Section 2.3),

CALIFORNIA RESEARCH AND TECHNOLOGY, INC.
PARAMETRIC STUDY CASES
DECELERATION VERSUS PENETRATION DEPTH

Double Penetrator Velocity
(3000 ft/sec)

Larger Penetrator
Diameter (9 in.)

Blunter Ogive (CRH=6)

Baseline Case
Dia = 6.5 in.
CRH = 9.25
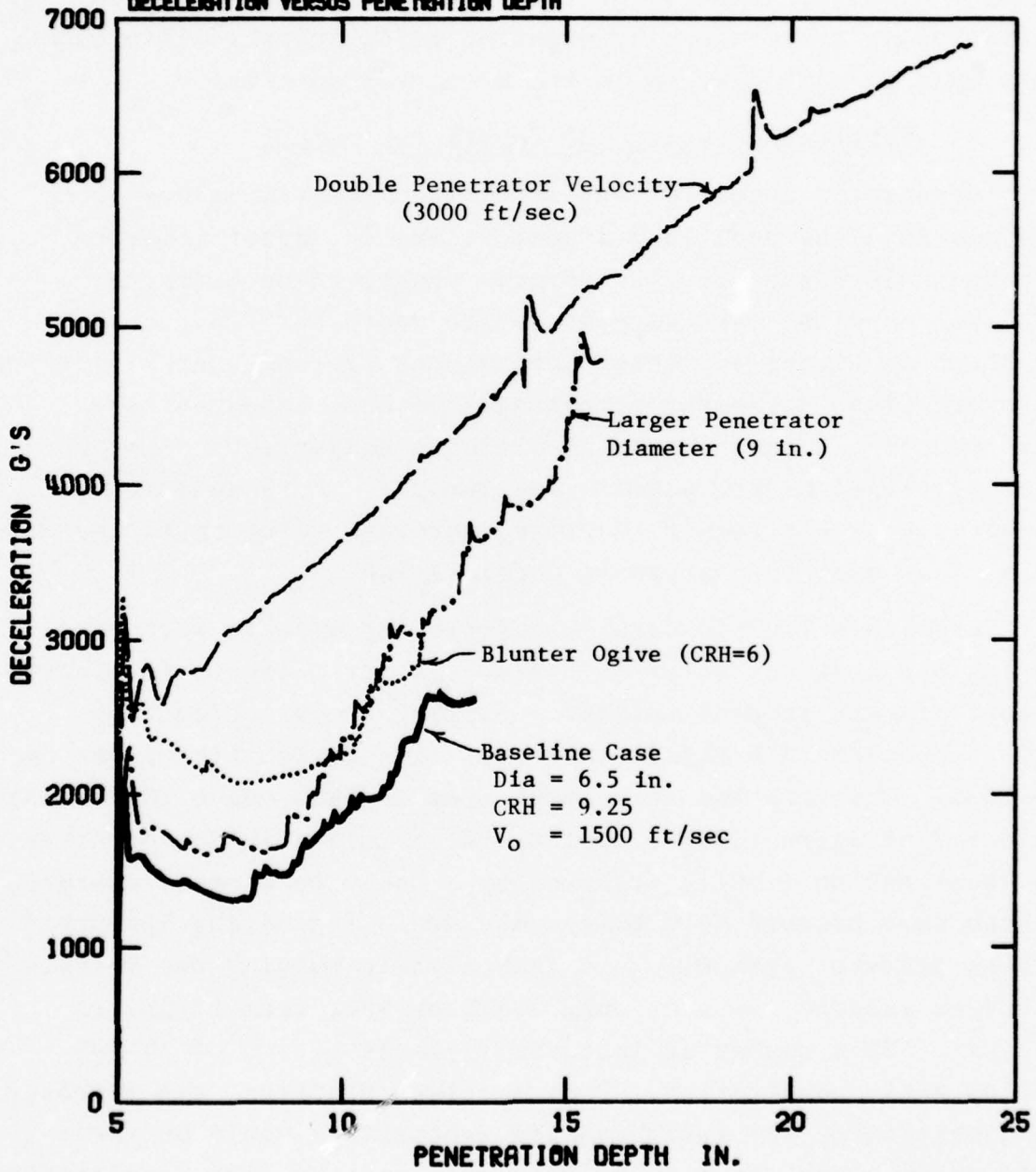V_o = 1500 ft/sec

DECELERATION G'S

PENETRATION DEPTH IN.

Figure 5. Comparison of Penetrator Deceleration vs Penetration Depth,
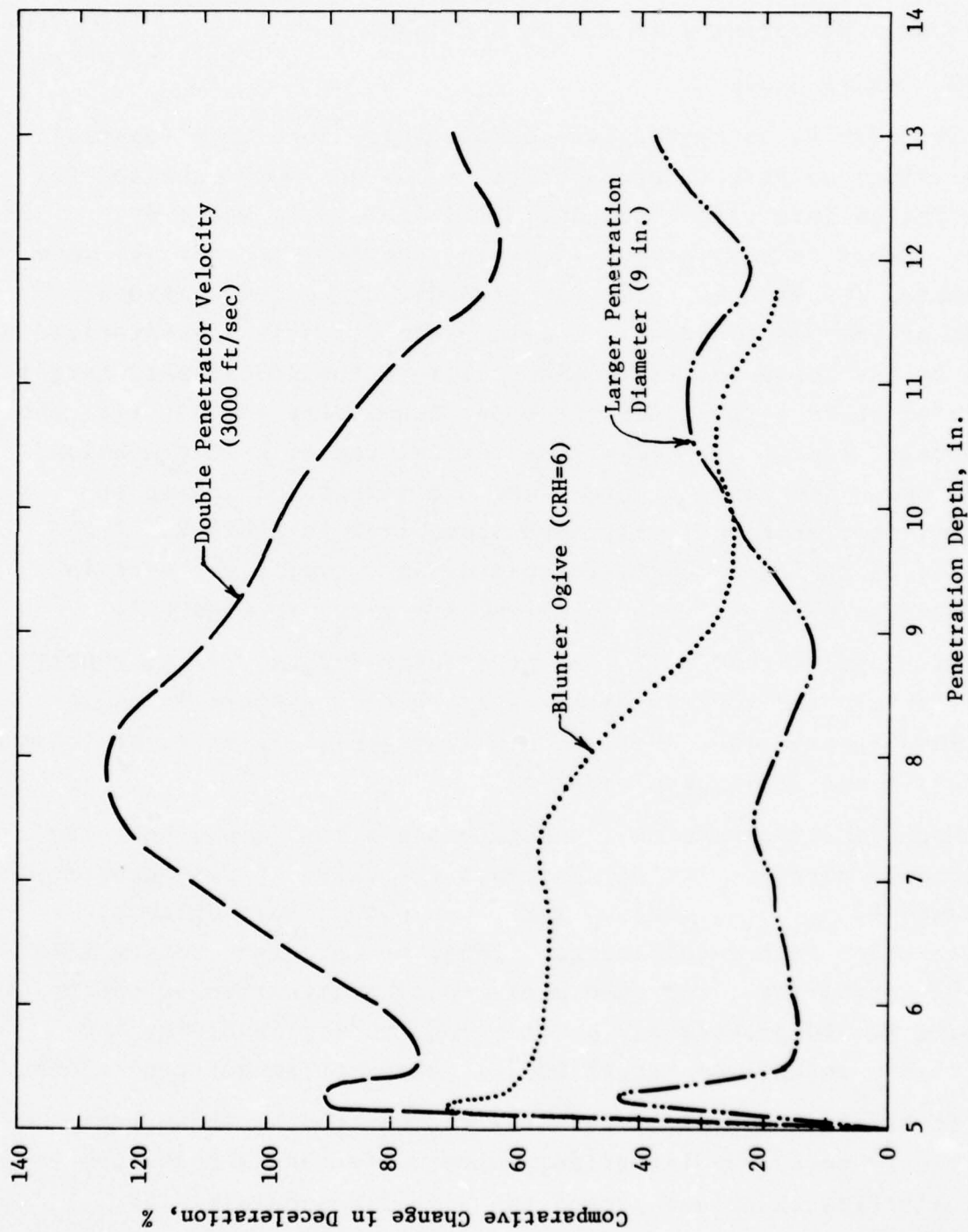Variations of Penetrator Parameters

14

Figure 6. Percentage Change (from Baseline Case) in Penetrator Deceleration vs Penetration Depth Due to Variations of Penetrator Parameters.

the observed increase in deceleration levels out at 110%, in reasonable agreement with simple scaling.

1.3.2 Zoning Study

The effects of Lagrangian computational zone size (spatial resolution) on results of numerical solutions were examined for penetration into sandstone, another softer rock, and a dry soil. Short code solutions (covering partial nose burial) were conducted for each of these target media using computational grids of varying fineness. Spatial resolution is characterized here by the number of Lagrangian cells in the *undisturbed* target material ahead of the penetrator per penetrator radius, i.e. the penetrator radius divided by the initial radial grid dimension, or $R_p/\Delta R_o$. The cases treated, and the effects of zoning on nominal deceleration levels, are summarized in Table 2. The effects of zoning on overall penetration dynamics, as seen in the average deceleration histories, are given in Figure 7.

Four undisturbed cells per penetrator radius are apparently satisfactory for rock targets. Where highly hysteretic media response is expected, such as in Watching Hill layer 1, at least six cells per radius are required.

Many factors, however, influence the stress field near the penetrator surface, including impact velocity and nose geometry. For example, blunter shapes, and those with abrupt changes, impose finer zone requirements. Thus, no universal zoning rule can be established, and some preliminary examination of zoning effects should precede any penetration studies involving sub-stantially unfamiliar target media, shape, or impact conditions.

It is also emphasized that the zoning results shown here apply only to Lagrangian grids, wherein the radial squeezing of cells flowing up and around the nose tip substantially

16

TABLE 2. CASES CONSIDERED IN ZONING STUDY

Penetrator: 400 lb, 6.5" dia Sandia design

Impact Velocity: 1500 ft/sec

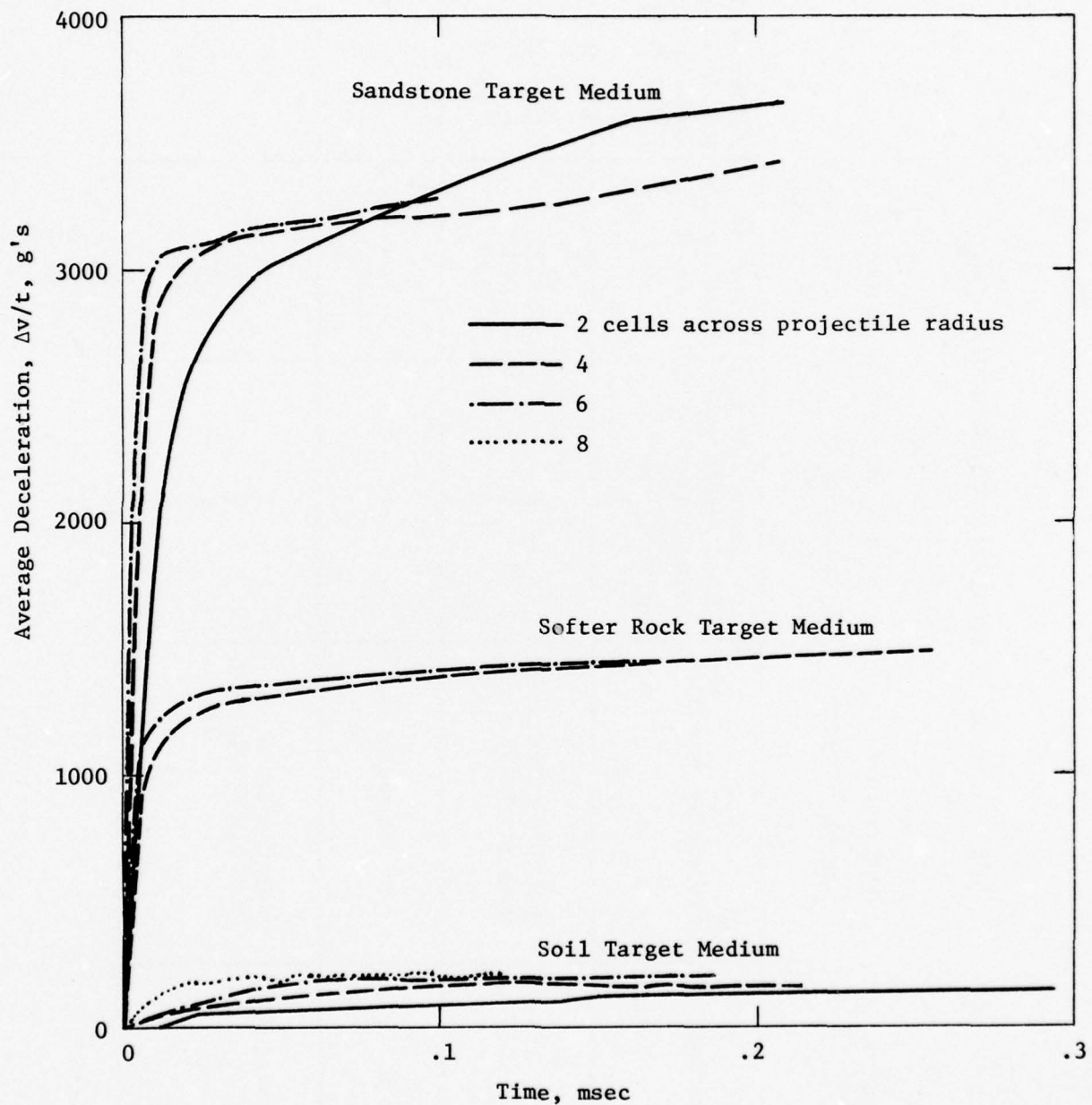| Target Material	Projectile Nose Tip	Zoning (Cells across penetrator radius, or $R_p/\Delta R_o$)	Nominal Deceleration Level, g's	Effect on Average Deceleration (as compared to $R_p/\Delta R_o=4$ case)
Sandstone	9.25 CRH ogive nose with tip beveled off	2 4 6	3350 3200 3300	+ 5% - + 3%
"Softer" Rock	9.25 CRH ogive nose	4 6	1450 1450	- 0%
Soil (Watching Hill Layer 1)	9.25 CRH ogive nose with tip beveled off	2 4 6 8	90 160 175 180	-44% - + 9% +13%

Figure 7.   Effects of Lagrangian Zone Size on Average Deceleration of
            Penetrator vs Time.   1500 ft/sec Impacts into Sandstone,
            Softer Rock, and Soil

increases the effective spatial resolution in that critical
stress region. Fixed (Eulerian) grids will require much
smaller cells (compared to the initial Lagrangian cell size)
to give the same effective resolution.

II. EFFECTS OF VARIATIONS OF TARGET AND PROJECTILE PARAMETERS ON PENETRATION DYNAMICS

To examine the sensitivity of earth penetration dynamics
to various projectile and target parameters, a series of
numerical solutions was performed wherein certain physical
parameters were independently varied. Results were compared
with the baseline case to determine the effects of the changes.

2.1 BASELINE PROBLEM CONDITIONS

For the baseline case, a full-scale penetrator impacting
a medium-strength rock at a representative EPW velocity was
selected. A relatively simple target material model was used,
so that changes in the model parameters would have discernible
physical significance.

The baseline problem conditions are summarized in
Figure 1 (page 6 in Section 1.2). The penetrator is the
DNA projectile used in recent full-scale field tests[7], except
that the tip of the ogive was not beveled.   The impact
velocity was 1500 ft/sec, and the target medium was sandstone.
The properties of this sandstone, which were arrived at in
consultation with Waterways Experiment Station (WES), are a
composite of values representing *typical* sandstones, rather
than a specific site or sample. The basic sandstone model
is described in Appendix A. The loading hydrostat stiffens
slowly but is strongly hysteretic. The model prescribes
highly dilatant behavior, particularly for the unloading
stress paths experienced in penetration problems.

A Mohr-Coulomb yield surface with a von Mises limit
was specified. It is modified by a strain softening "frac-
ture" model, wherein the post-fracture material strength
is gradually degraded as a function of generalized plastic

20

strain. This new model is similar to the one developed for analysis of a penetration test into welded tuff. Observations following penetrations into rock have shown that there is a region of highly comminuted rock surrounding the penetrator and the penetrator hole. Beyond the comminuted region, there are successive annular zones of brecciated and sheared rock, with the degree of fracture diminishing with increasing radius. Since the fractured rock will generally have reduced shear and tensile strengths, it is important that the material model reflect this mechanism. Accordingly, a material model was developed which included relations to assess the *degree* of failure which has occurred, and to degrade the rock properties appropriately. Development of this model is discussed in Reference 3.

In the new post-fracture model, material reaching the failure (yield) surface specified for the *intact* material begins to fracture. Subsequent increases in the generalized plastic strain, $\bar{\varepsilon}_p$, cause degradation of the yield surface, according to the relation

$$Y_{dgd} = Y(1 - 10\bar{\varepsilon}^p)$$

where Y is the intact *yield* surface and Y_{dgd} is the degraded (post-fracture) yield, and

$$\bar{\varepsilon}^p = \int (\tfrac{2}{3} de_{ij}^p de_{ij}^p)^{\frac{1}{2}}$$

As soon as the degraded yield strength drops to the value given by the yield surface, Y_{min}, that is assigned for completely crushed material, the degradation is complete and the material thereafter has the properties of the crushed material.
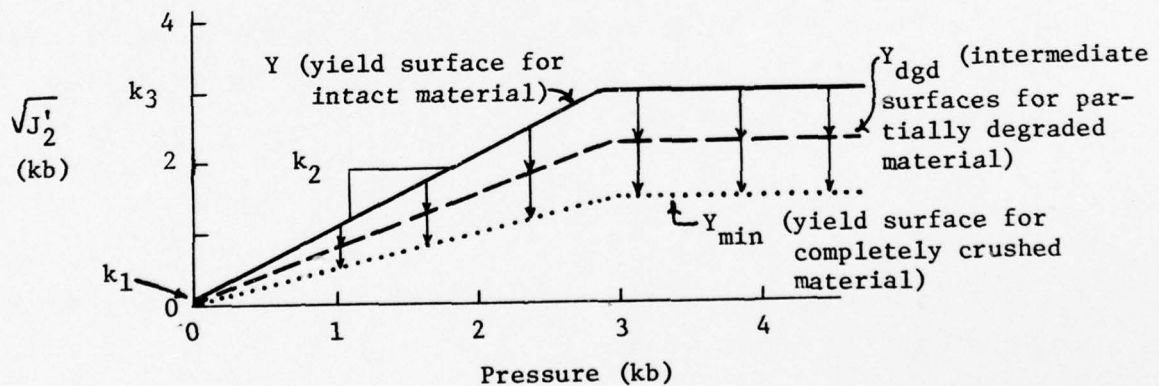
21

The yield surfaces assumed for the intact and completely crushed sandstone were:

$$\sqrt{J_2'} = \text{Min } (k_1 + k_2 P, \ k_3)$$

where the values of the constants are:

	Intact	Crushed
k_1 ("cohesion", i.e., P=0 intercept)	.1 kb	0
k_2 (slope)	1	.5
k_3 (Mises limit)	3 kb	1.5 kb

These yield surfaces are shown in the accompanying sketch.

The friction rule used to compute the shear stress (τ) at the penetrator/target interface was:

$$\tau = .15 \sqrt{J_2'} \ (\sigma_n)$$

(Here the normal stress, σ_n, is put into the yield function equation for $\sqrt{J_2'}$ given above.)

22

Figure 8 shows the initial Lagrangian grid for the physical parameter study. There are 4 undisturbed Lagrangian cells per projectile radius. For efficiency in this series of solutions, the penetrator nose tip was initially buried 5-in. into the target. This allows the solution to bypass the early stages of the impact analysis, which are generally uninteresting in axisymmetric impacts of pointed projectiles because only a relatively small region of target and projectile are involved and the acceleration forces are correspondingly small. When the partially-buried nosetip solutions begin, there are spurious acceleration excursions due to inertial factors, but they damp out quickly and the subsequent acceleration levels are reasonable for comparable depths of penetration.

2.2 PHYSICAL PARAMETER STUDY CASES

Parameters in several categories were selected for consideration in the study. Only one basic parameter was changed for each case. The change in the value of the parameter was generally significant, such as half or twice the baseline case value. The cases are summarized in Table 1 (page 10 in Section 1.3). Additional description is given in the following:

o Yield surface (changes refer both to intact and crushed yield surfaces)

Case 2080-60   - <u>Mises limit</u> - decrease by 50%:

$$k_3 = 1.5 \text{ kb} \qquad k_3^{min} = .75 \text{ kb}$$

Case 2080-61   - <u>Mises limit</u> - increase by 100%:

$$k_3 = 6 \text{ kb} \qquad k_3^{min} = 3 \text{ kb}$$

23

CALIFORNIA RESEARCH AND TECHNOLOGY WAVE-L CODE
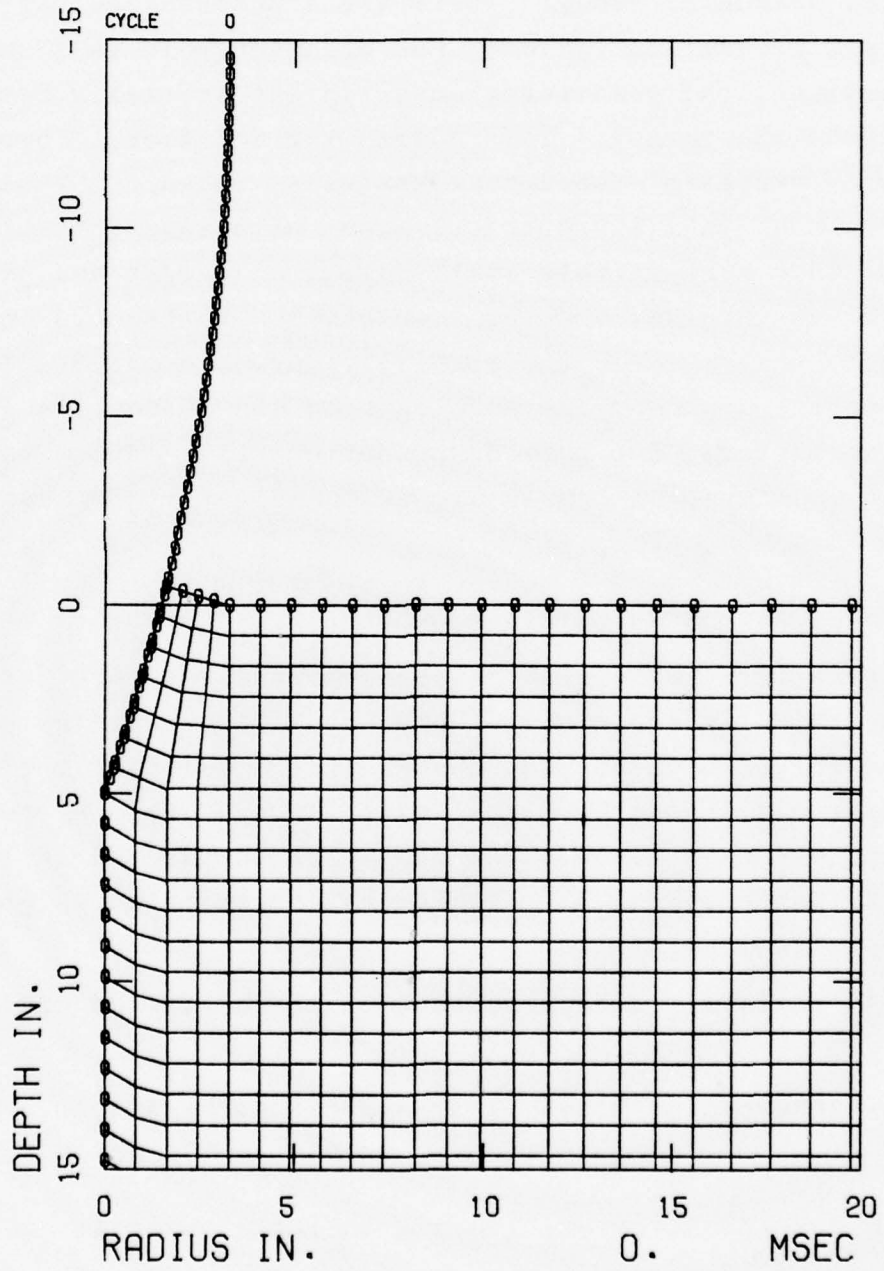

Figure 8. Initial Computational Grid for Physical
Parameter Study Cases

24

Case 2080-62 — <u>Slope</u> - decrease by 50% and adjust k_1 such that unconfined compressive strength remains unchanged:

$$k_1 = .1683 \text{ kb} \qquad k_2 = .5 \qquad k_2^{min} = .25$$

Case 2080-65 — <u>Unconfined compressive strength</u> - increase by 100% to .82 kb (also equivalent to increasing k_1, or "cohesion," by 100%:

$$k_1 = .2 \text{ kb}$$

The yield surfaces resulting from the above variations are shown in Figure 9.

o <u>Hydrostat</u>

Case 2080-70 <u>Bulk modulus</u> - increase by 100% and adjust other constants in hydrostat equations as required for compatibility:

$$K_0 = 80 \text{ kb} \qquad K_o' = 100 \text{ kb} \qquad a = .4$$

o <u>Friction</u>

Case 2080-82 <u>Coefficient of friction</u> - set to zero (frictionless interface condition)

o <u>Target density</u>

Case 2080-100 <u>Normal density</u> - increase by 100%:
$$\rho_o = 4$$

o <u>Impact velocity</u>

Case 2080-110 <u>Initial velocity</u> - increase by 100%:
$$V_o = 3000 \text{ ft/sec}$$

o <u>Penetrator shape and size</u>

Case 2080-120 <u>Nose radius of curvature</u> - decrease CRH $\approx 35\%$ to give blunter ogive:

CRH = 6 (nose radius = 39 in.)

Case 2080-122 <u>Penetrator diameter</u> - increase $\approx 50\%$:

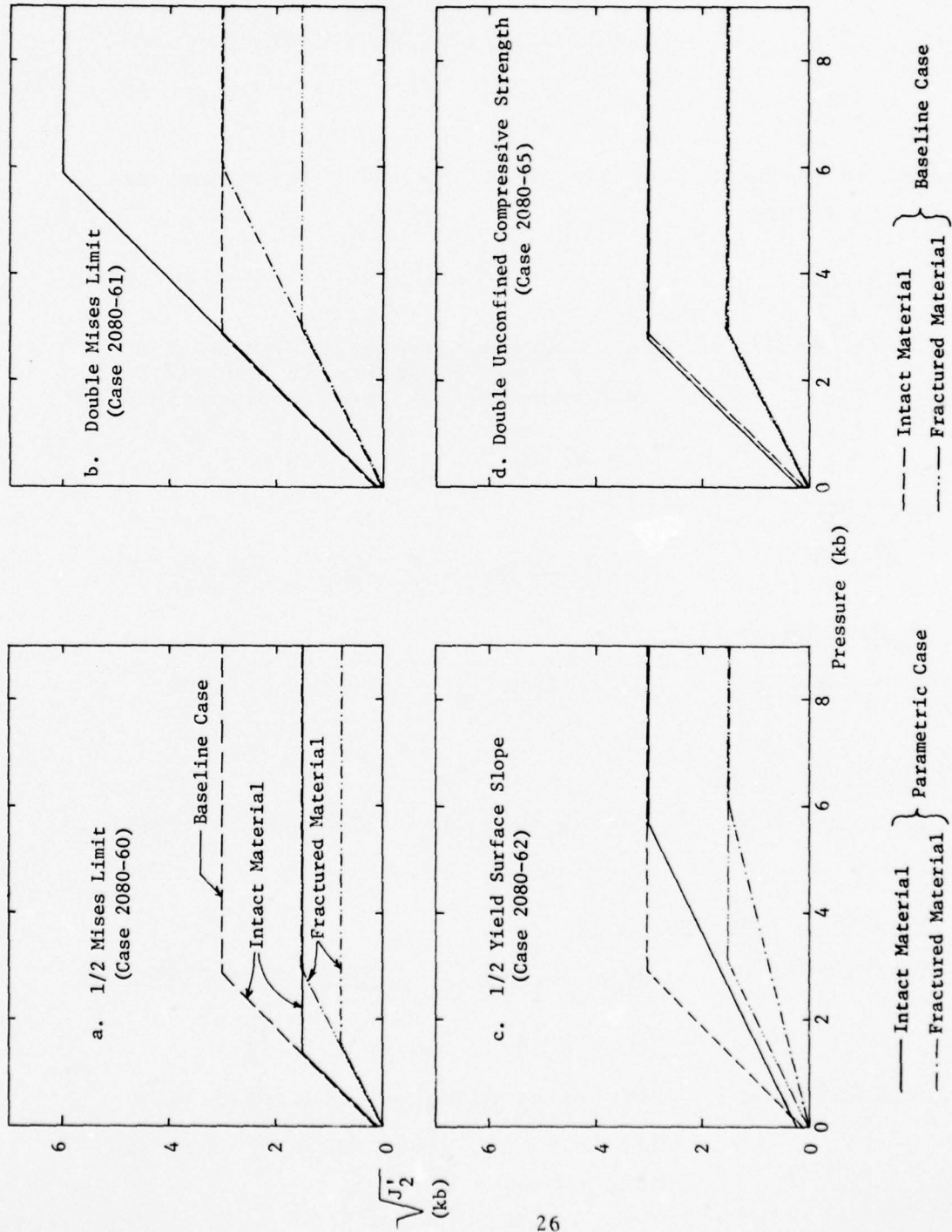Dia_p = 9 in., gives W/A = 6.3 psi and nose radius = 83.25 in.

Figure 9. Variation of Yield Surface Parameters

2.3   COMPARATIVE RESULTS

2.3.1   Penetrator Rigid-Body Decelerations

Figure 10 compares the penetrator deceleration histories from the solutions of all target media parameter cases with the baseline case. Figure 4 (page 12 in Section 1.3) compares these same cases on the basis of the percentage change (from the baseline case) in the time-averaged deceleration, $\Delta v/t$, vs time, t.

a.   Yield Surface

Lowering the higher pressure portion of the yield surface by halving the Mises limit results in a reduction of the deceleration of about 20%. Raising this portion of the yield surface by doubling the Mises limit results in a 5 to 10% increase in deceleration. Note, from Figures 9a and 9b, that halving the intact Mises limit only affects stress states where the pressure is greater than 1.4 kb and the deviatoric stress $\sqrt{J_2'}$ is at least 1.5 kb; doubling the Mises limit only affects stress states where the pressure is greater than 2.9 kb and the deviatoric stress $\sqrt{J_2'}$ is greater than 3 kb. Thus, lowering the yield surface influences a greater volume of material near the penetrator, and for longer times than raising the yield surface. This can be seen in Figure 11, which shows contours of the pressure in the sandstone around the penetrator. The Mises limit is an important parameter if the pressures near the penetrator surface are high enough to activate this limit on the yield surface. This is more likely to be the case in media with a low Mises limit and/or where the penetrator nose is blunt and the velocity is high. (The Mises limit, of course, is a parameter only in certain plasticity models, and it was used here for simplicity. Other models generally have some equivalent form which limits the yield strength at high pressures.)
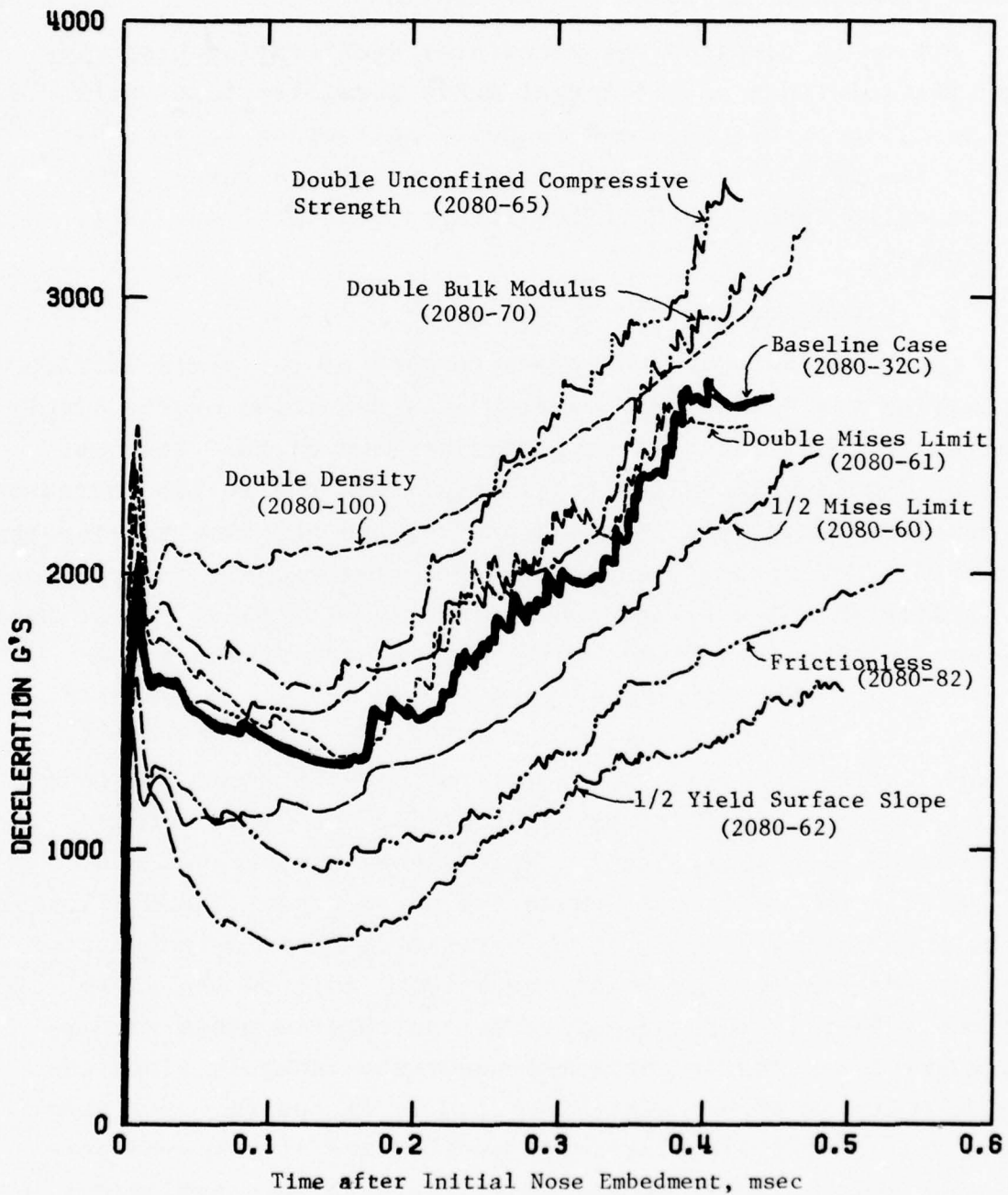
27

Figure 10. Comparison of Penetrator Deceleration Histories, Variations in Target Media Parameters

RUN NO. 2080-52C, PENETRATION INTO SANDSTONE
PRESSURE CONTOURS
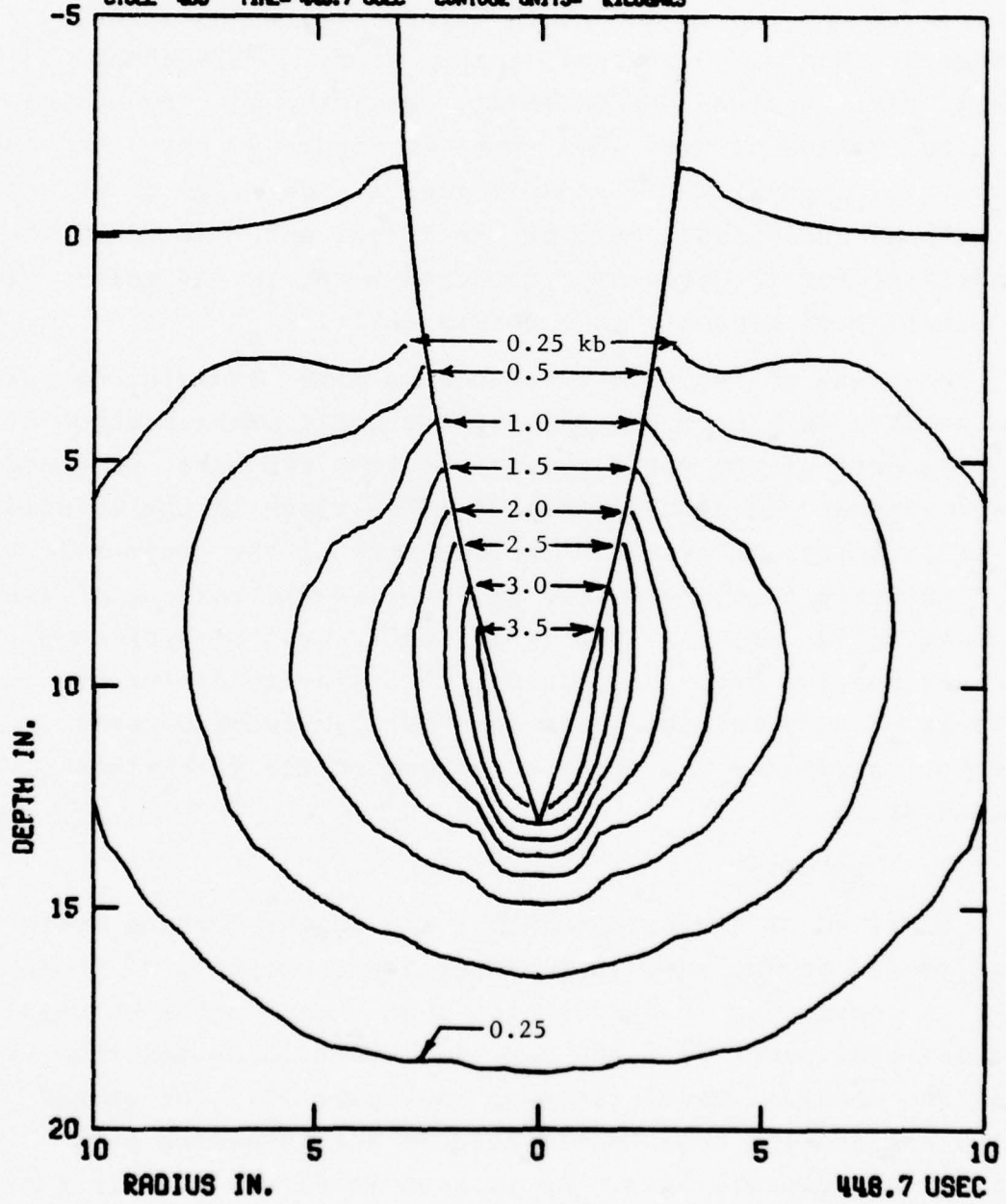CYCLE 469   TIME= 448.7 USEC   CONTOUR UNITS= KILOBARS

Figure 11.   Contours of Pressure in Sandstone, Baseline
Penetration Case.

29

Halving the slope of the yield surface while retaining the same unconfined compressive strength caused the largest effects of all the target media stress-strain and strength parameter changes considered in this study. This change considerably weakens the material, resulting in a reduction of deceleration of over 40%. Note in Figure 9c that the yield surface is significantly reduced over a wide range of pressures. This range encompasses much of the target material near the penetrator for the problem considered here, so the major effect on penetration dynamics is understandable.

Doubling of the unconfined compressive strength, or, as can be seen in Figure 9d, raising the entire Mohr-Coulomb or sloping part of the yield surface by just 100 bars, produced a 25% increase in deceleration at later times in the solution. At early times, material in the vicinity of the projectile is at relatively high pressures, and the 100 bar raising of the sloping yield surface is insignificant. As the shock wave weakens and the material unloads, the relative difference in strength due to the change in the yield surfaces becomes greater, producing the observed effect on the later-time decelerations.

b. Hydrostat

Doubling of the bulk modulus, K_o, in the loading hydrostat causes an increase in penetrator deceleration of 10 to 15%. A comparison of hydrostatic load-unload paths between the material model with the doubled bulk modulus and the baseline material model is shown in Figure 12. The unload paths reflect the adjustments made to the unloading parameters for compatibility. As is seen in Figure 4, this substantial change in the equation of state caused only a relatively small change in the penetrator dynamics. This is a favorable trend for EPW development because:
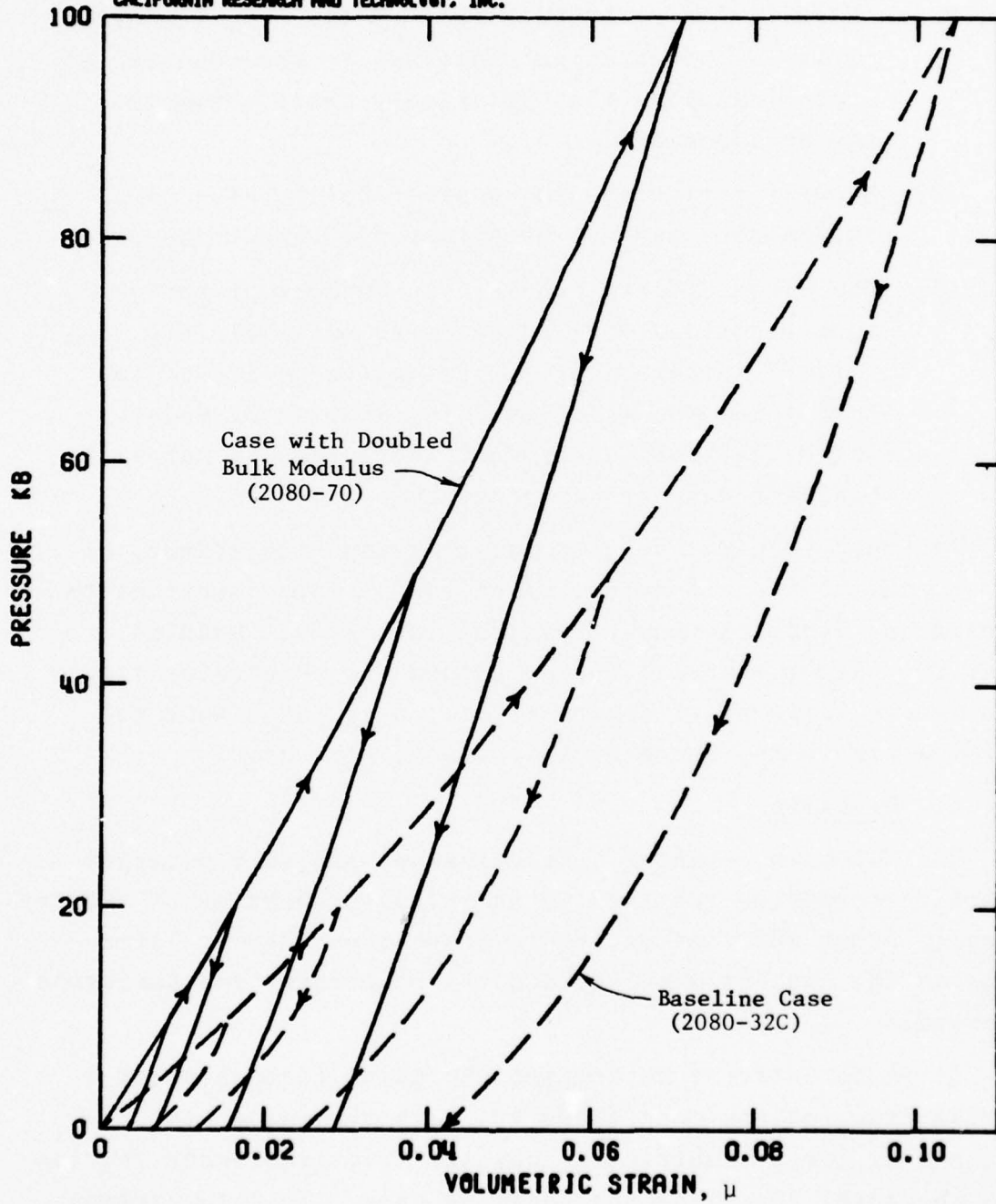
30

Figure 12. Comparison of Hydrostatic Load-Unload Paths between Case with Doubled Bulk Modulus ($K_o=80$ kb) and Baseline Case ($K_o=40$ kb)

31

(1) In predictive and design analyses, it will generally be necessary to rely on estimates of the equations of state for real EPW target media. The insensitivity of penetration processes to the equation of state indicates that relatively crude estimates may be adequate.

(2) Natural variations in compressibility at a given target site may not be a factor of great concern.

(3) The large efforts required to conduct property investigations of a target site material (e.g., seismic surveys, coring, extensive series of lab tests) and the associated formulation of models which faithfully reproduce lab curves of material behavior may not be necessary.

It would be very useful to also examine the effects of changes in the shear modulus, which may be more important to penetration dynamics than variations in the bulk modulus, since the target material forced around the penetrator tip experiences large shear deformations. Such cases were not included within the scope of this study, however.

c. Friction

The solution assuming a frictionless projectile/target interface condition resulted in an initial reduction of deceleration of about 20%, increasing to a 40% reduction at later times as the contact area between the penetrator and sandstone enlarged.

It is of interest to compare the axial force history for the frictionless case (2080-82) with the force history obtained by simply subtracting out the frictional contribution from the total force for the baseline case. This comparison is shown in Figure 13. The true frictionless case lies
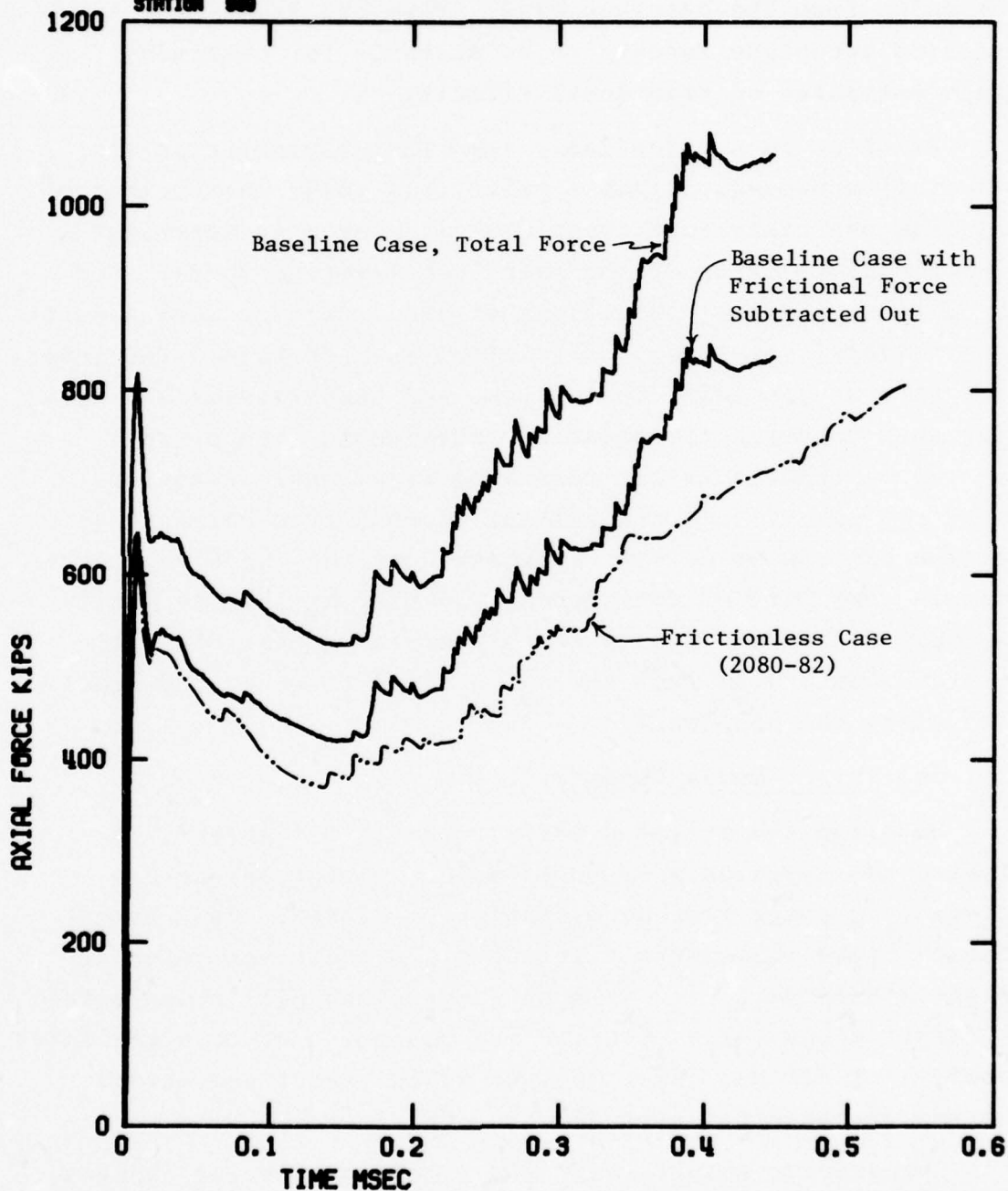
Figure 13. Comparison of Axial Force History from Frictionless Case with Estimated Axial Force History Obtained by Subtracting Frictional Force Component from Total Force in Baseline Case

33

somewhat below the curve obtained by subtracting the frictional component from the baseline case. However, the simple subtraction technique appears to be suitable for obtaining rough estimates of frictional effects.

Friction is a potentially important parameter in the penetration process, since a relatively small coefficient of friction can cause sufficient dragging force to represent a significant fraction of the total decelerating force. For the complex physical conditions at the interface during earth penetrations, the amount of friction is uncertain. The interface stresses, sliding velocities, and temperatures are very high when compared to conditions obtainable with present laboratory techniques for measuring frictional parameters. Post-test surveys and analysis of records from earth penetration tests provide some indication of this problem. For example, evidence of considerable heating at the projectile surface is seen after some tests wherein patches of metal film and comminuted rock have been fused together and deposited along the hole wall.[9]

d.   Target Media Density

Doubling the target density, from 2 to 4 gm/cm^3, increased the resistance to penetration, giving an average increase in penetrator deceleration of 20-40%. This hypothetical case represents a relatively extreme variation in target massiveness, and is much larger than will be expected in target media for a specific EPW design. For more realistic density variations, like ±25%, we would expect acceleration changes of the order of ±10%.

Comparative results from the cases considering changes in impact and penetrator design parameters are presented in Figure 14 and Figure 5 (page 14 in Section 1.3) in terms of
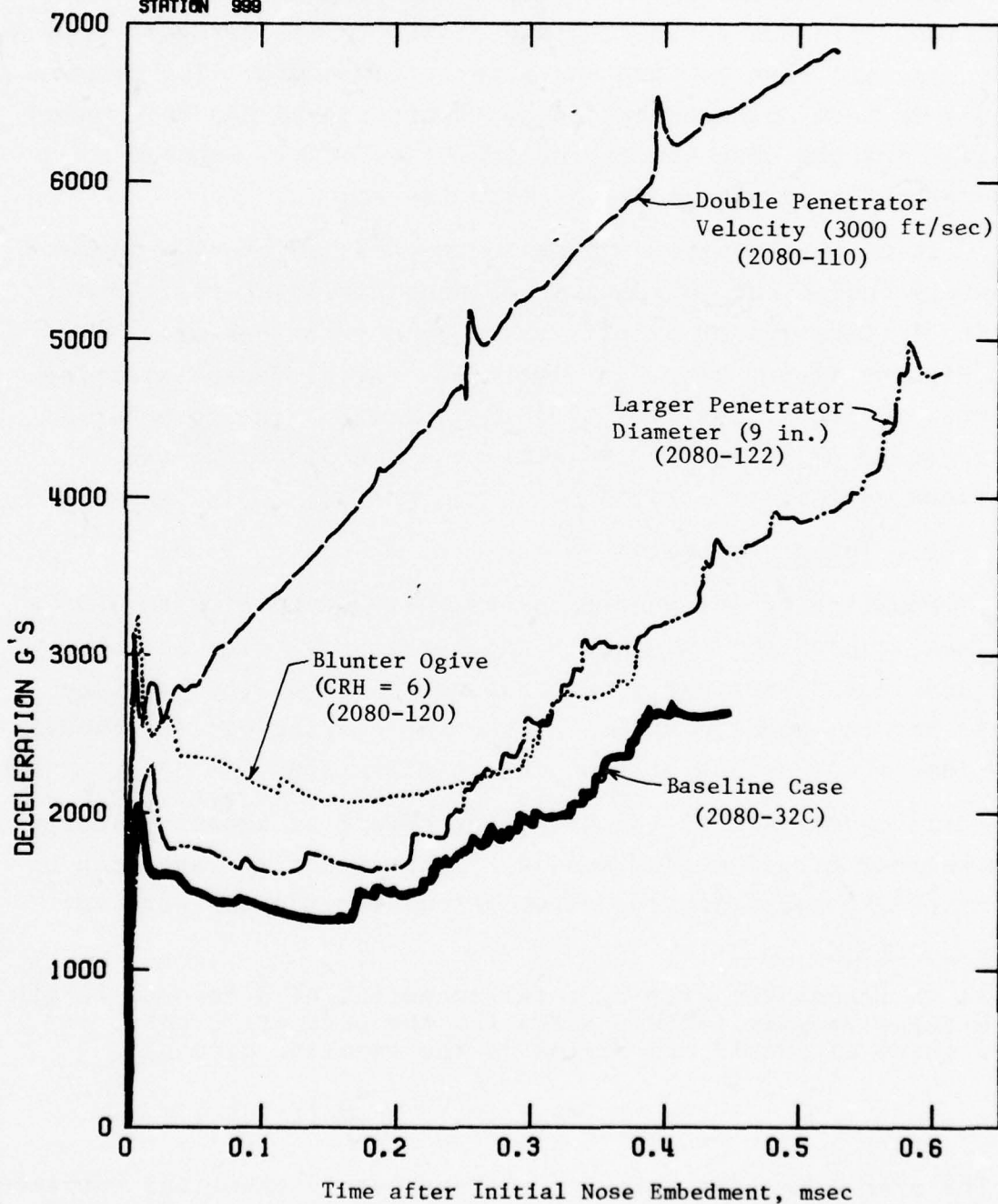
Figure 14. Comparison of Penetrator Deceleration Histories, Variations in Penetrator Parameters.

35

penetrator deceleration vs time and penetrator deceleration
vs depth of penetration. Figure 15 and Figure 6 (page 15 in
Section 1.3) show the percentage change in deceleration from
the baseline case vs time and penetration depth. The compar-
isons in terms of penetration depth are considered more mean-
ingful for the case concerning impact velocity, since the
amounts of nose embedment are then the same.

It is also possible to scale the time to provide approx-
imately equivalent percentages of nose embedment for these
cases.* Comparative results using this technique are shown
in Figures 16 and 17. (In Figure 16, the different starting
times are due to the fact that the initial 5-in. nose burial
represents different percents of nose embedment for the
various penetrator designs.)

   e. Impact Velocity

Doubling of the penetrator velocity, from 1500 to 3000
ft/sec, caused an increase in deceleration varying between
60 and 130% during early penetration. Neither the baseline
case nor the doubled velocity case was carried out far enough
to show a comparison of the peak decelerations.

An indication of the differing effect of impact velocity
in another target medium and in a lower velocity range can be
obtained by comparing two other calculations which were not

---

* At an impact velocity V, total embedment of a nose of length
  L takes roughly $t=L/V$. Times for the parametric cases in
  Figures 16 and 17 are scaled to the baseline case by

$$t_{scale} = t' \frac{L/V}{L'/V'} - \frac{d_o}{V} \left(1 - \frac{L}{L'} \right)$$

  The primed factors refer to the parametric case, the unprimed
  factors refer to the baseline case, and d_o is the depth of
  initial embedment (5 in.).

36

Figure 15. Percentage Change (from Baseline Case) in Deceleration
vs Time, Variations of Penetrator Parameters.

37

Double Penetrator Velocity
(3000 ft/sec) (2080-110)

Blunter Ogive   (CRH = 6)
(2080-120)

Larger Penetrator
Diameter (9 in.)
(2080-122)

Baseline Case
(2080-32C)

Deceleration, g's

7000

6000

5000

4000

3000

2000

1000

0
-.1   0   .1   .2   .3   .4   .5   .6   .7   .8   .9   1.0   1.1   1.2

Scaled Time after Initial Nose Embedment, msec

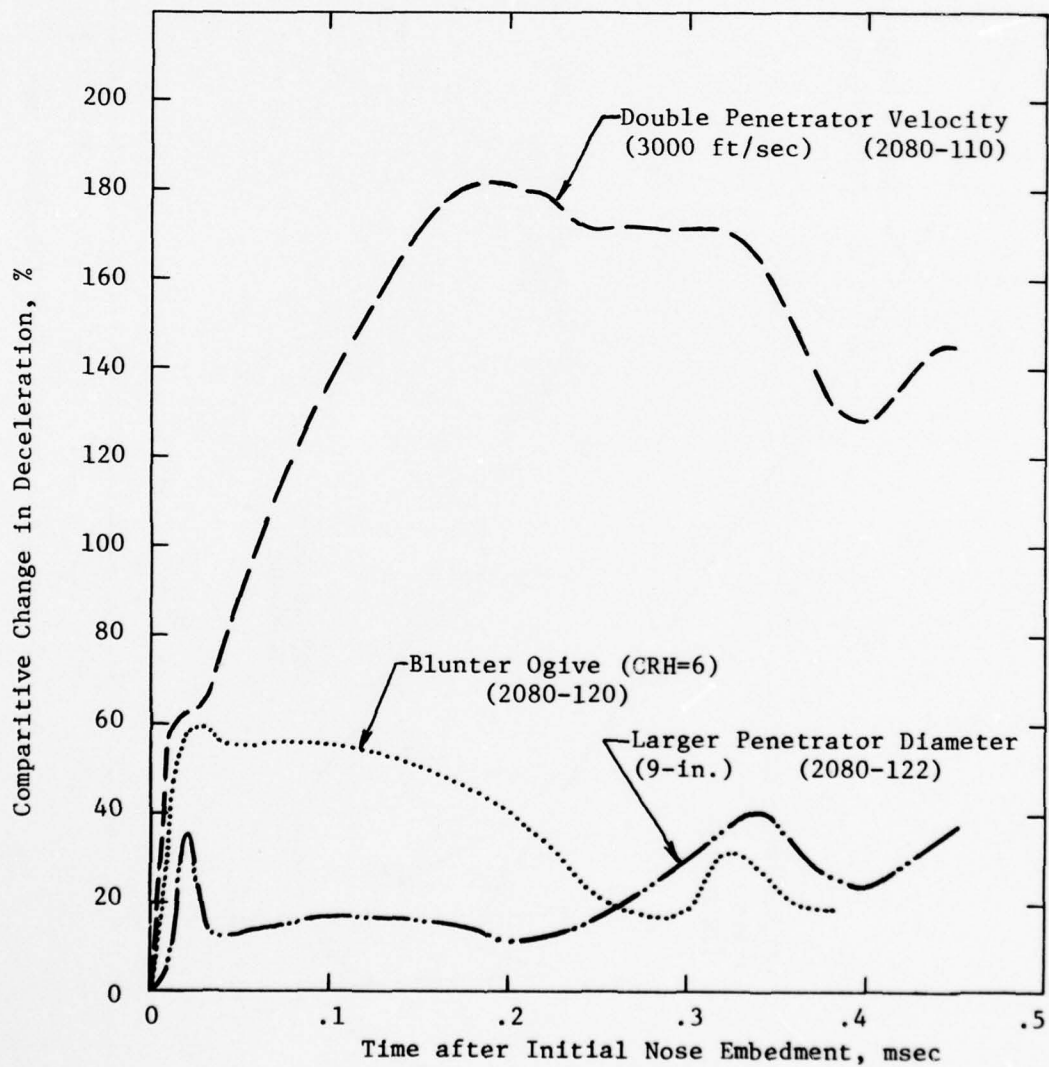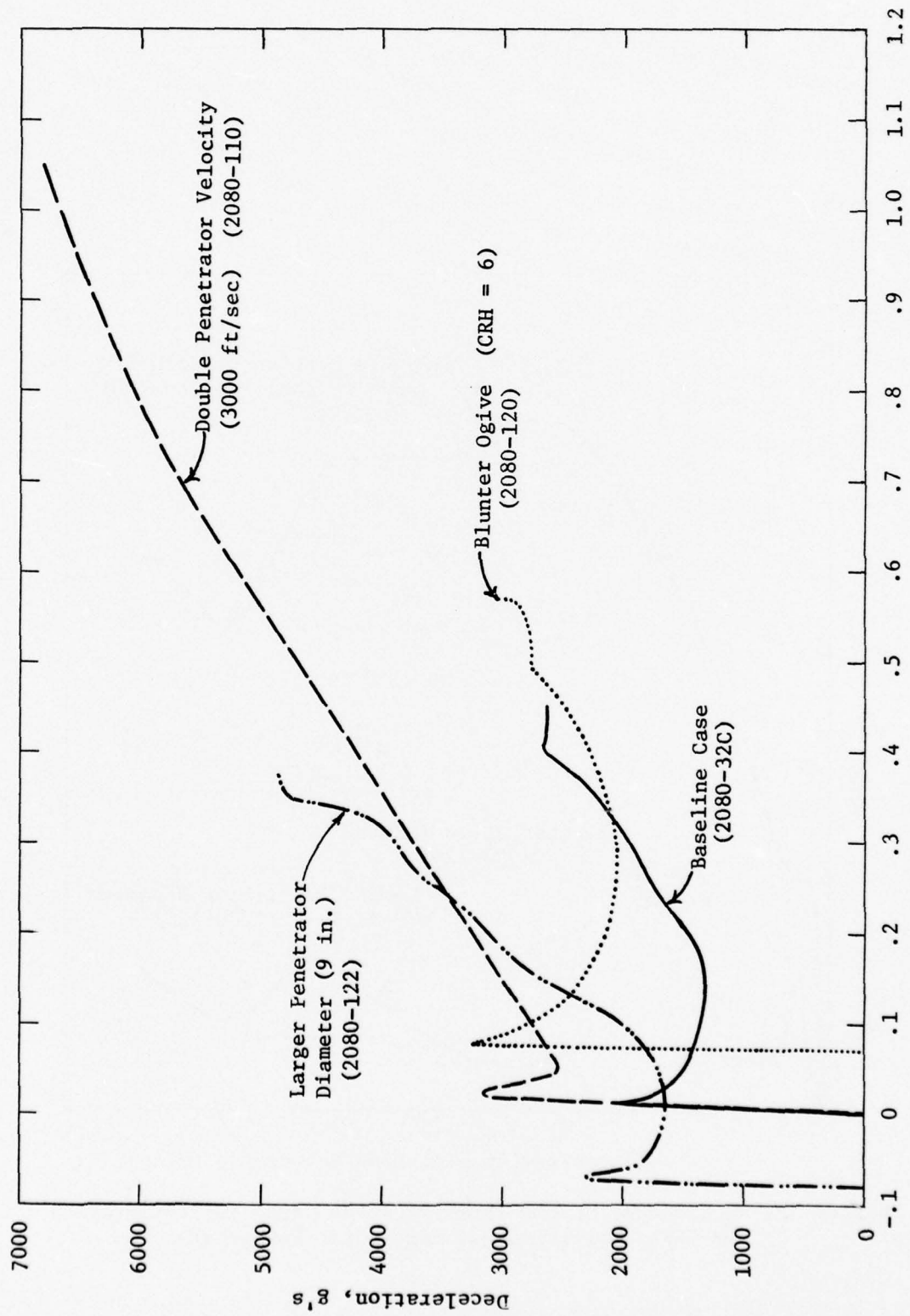Figure 16. Comparison of Penetrator Deceleration Histories, Variations in Penetrator Parameters
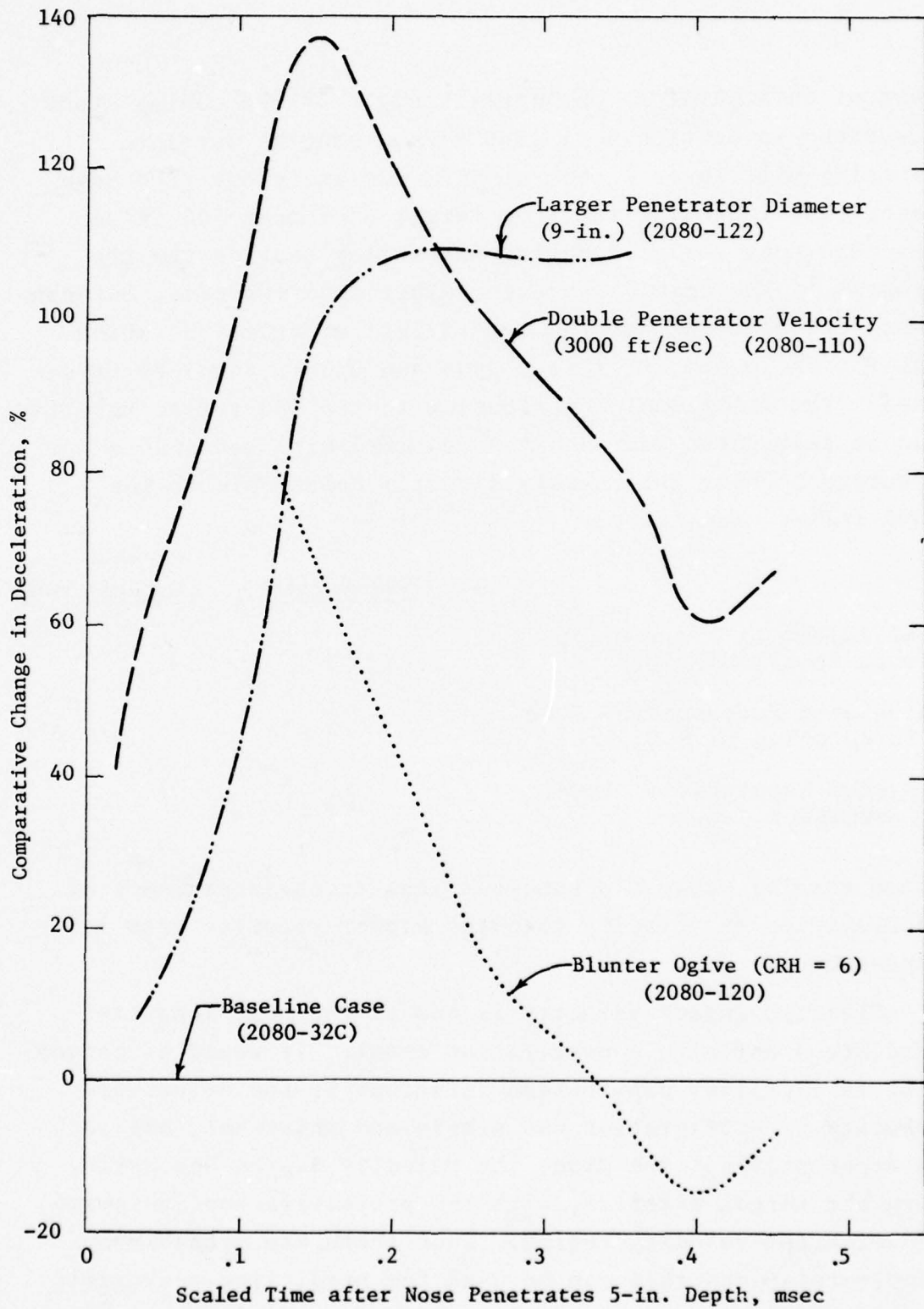
38

Figure 17. Percentage Change (from Baseline Case) in Deceleration vs Scaled Time, Variations of Penetrator Parameters

part of this physical parameter study. In the zoning study
described in Section 3, a 1500 ft/sec penetration into
Watching Hill layer 1 soil at DRES was analyzed. The same
penetrator impacting the same target medium at 500 ft/sec
has also been analyzed during an earlier task on the EPW
program.[1] The only difference, other than velocity, between
these calculations was the coefficient of friction, which
was 0.6 in in the 500 ft/sec case and 0.3 in the 1500 ft/sec
case. The frictional contribution to the 500 ft/sec results
can be segregated and adjusted downward with reasonable
accuracy to make the results directly comparable to the
1500 ft/sec case; i.e.,

	500 ft/sec	1500 ft/sec
Coefficient of friction, μ, used in calculations	0.6	0.3
Calculated acceleration level in Watching Hill Layer 1	110 g's	170 g's
Adjusted acceleration level, assuming μ = 0.3	80 g's	---

These results suggest a somewhat less strong dependence of
acceleration on velocity than the higher velocity case in
sandstone.

Clearly, impact velocity is one of the most important
parameters defining a penetration event. It would be conven-
ient in empriical penetration relations if the effect of
velocity on acceleration was simple and universal, but such
is apparently not the case; the velocity dependence varies
with the target material, with the projectile configuration,
and with the velocity regime. Thus there are probably no
simple relations that can be used for predicting peak rigid
body accelerations over a wide range of conditions.

f. Penetrator Shape and Size

Changing the nose shape to a blunter ogive by changing
the radius of curvature from CRH=9.25 to CRH=6, produced an
initially large increase (60%) in penetrator deceleration,
followed by a decay to 20-30% difference as more of the nose
became engaged with the target. The penetrator weight and
diameter were not changed for this comparison. The nose
length is 15.6 in. for the CRH=6 case, as compared to 19.5 in.
for the CRH=9.25 baseline case.

Increasing the penetrator diameter to 9 in. produced
about 110% greater penetrator deceleration after the noses
were half-embedded. Since the penetrator weight was held
constant, this reduced the sectional load nearly in half, from
a W/A = 12 psi to a W/A = 6.3 psi. The nose CRH was held con-
stant at 9.25. The computed increase in deceleration is in
line with what would be expected from simple scaling consid-
erations, which would predict a 92% increase.

g. Other Parametric Comparisons

In addition to the cases described above, some explor-
atory information on other parameters was gained through
comparisons among the zoning study solutions and trial solutions
conducted to arrive at the baseline conditions.

o *Penetrator Nose Tip Shape*. The DNA penetrator
   referred to in this report has a small conical
   nose tip, giving, in cross-section, a beveled
   tip to the ogive nose. The conical tip has a
   45° half-angle and is .5 in. long. For some
   field events, a nose cap has been secured to
   the tip to give a two-piece pointed ogival nose.
   Comparisons of the effect on penetration dynamics
   between the pointed and beveled designs were made
   by comparing code solutions from the zoning and
   parametric studies using the two designs.

41

Average deceleration histories for penetrations
at 1500 ft/sec into two materials, Watching Hill
Layer 1 soil and sandstone, are shown in Figure 18.
(The sandstone model in this comparison was the
one used in the zoning study (described in Section
III and Appendix A); it differs from the baseline
case in the physical parameter study in its
treatment of fracture and in the coefficient
of friction, using 0.3 instead of 0.15.) The
computational zoning was 6 cells per projectile
radius for the soil cases and 4 cells per pro-
jectile radius for the sandstone cases. The
beveled nosetip design induces ~25% greater
deceleration for both of these penetration
conditions. This result indicates that the
detail of the nose tip design is an important
factor in the forces applied to the penetrator
and the resultant decelerations.

There is a possibility that target material can
locally separate from the projectile near the
point of the bevel/ogive intersection. In these
calculations, separation at any point could occur
if the normal stress in the target acting on the
penetrator was zero or tensile. Otherwise, the
target material was assumed to remain in contact
with the penetrator. Separation at the bevel/
ogive intersection using this criterion did not
occur in these calculations. Additional studies
would be needed to investigate the possible
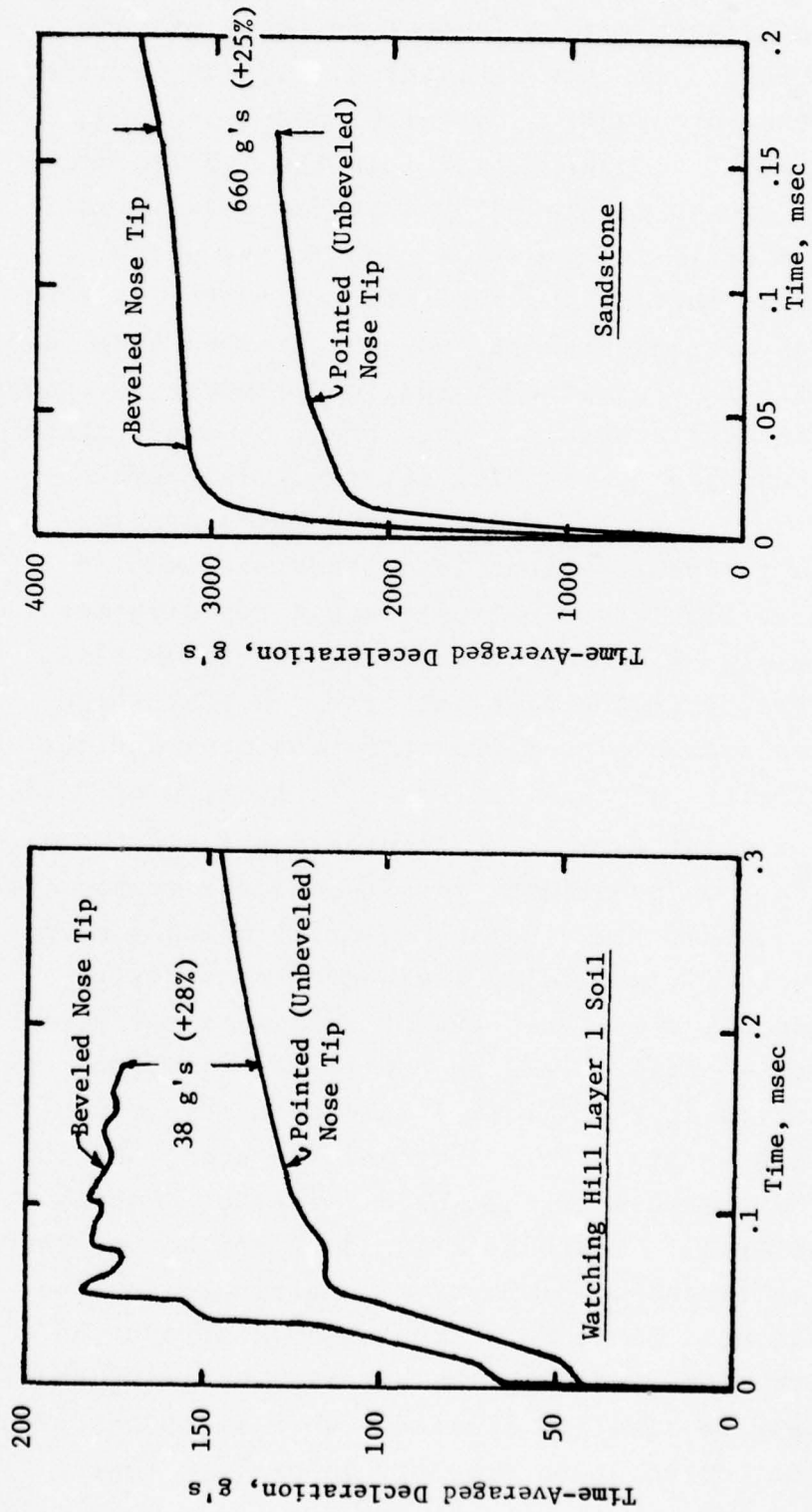effects of geometric separation.

Figure 18. Comparisons of Time-Averaged Deceleration of Penetrator vs Time between Beveled and Unbeveled Nose Tip for Penetrations into Soil and Sandstone at 1500 ft/sec

43

o *Dilatancy*. Dilatant behavior is commonly observed
during stress-strain laboratory tests of rock
materials. If this behavior significantly affects
penetration dynamics, material models should
attempt to account for it. In the models, dila-
tancy can be simulated by using an associated
flow rule in the model of plasticity, which
produces increments of plastic volumetric strain.
Use of a Prandtl-Reuss (non-associated) flow rule
assumes that plastic distortion produces no change
in volumetric strain. The effect on penetration
of a material exhibiting dilatancy is shown in
Figure 19, which compares the average deceler-
ation for penetrations into sandstone modeled
both as a dilatant material and a non-dilatant
material. (The sandstone model for these cases
differed from the baseline case in that there
was no fracture/post-fracture treatment and the
coefficient of friction was 0.3, instead of 0.15.)
The dilatant material case provides a significant
increase in penetrator resistance; the reason for
this is that the dilatant material unloads much
more slowly, providing a higher stress distri-
bution all along the contact area with the pene-
trator surface. This is due to the dilation
occurring as the material undergoes severe dis-
tortion as it is forced around the nose, holding
up the pressure in the solid (elastic) component
of material. Where dilation does not occur, the
entire expansion of material contributes to the
unloading. Since this process does affect the
penetration dynamics, the material modeling should
attempt to simulate dilatancy when it is observed
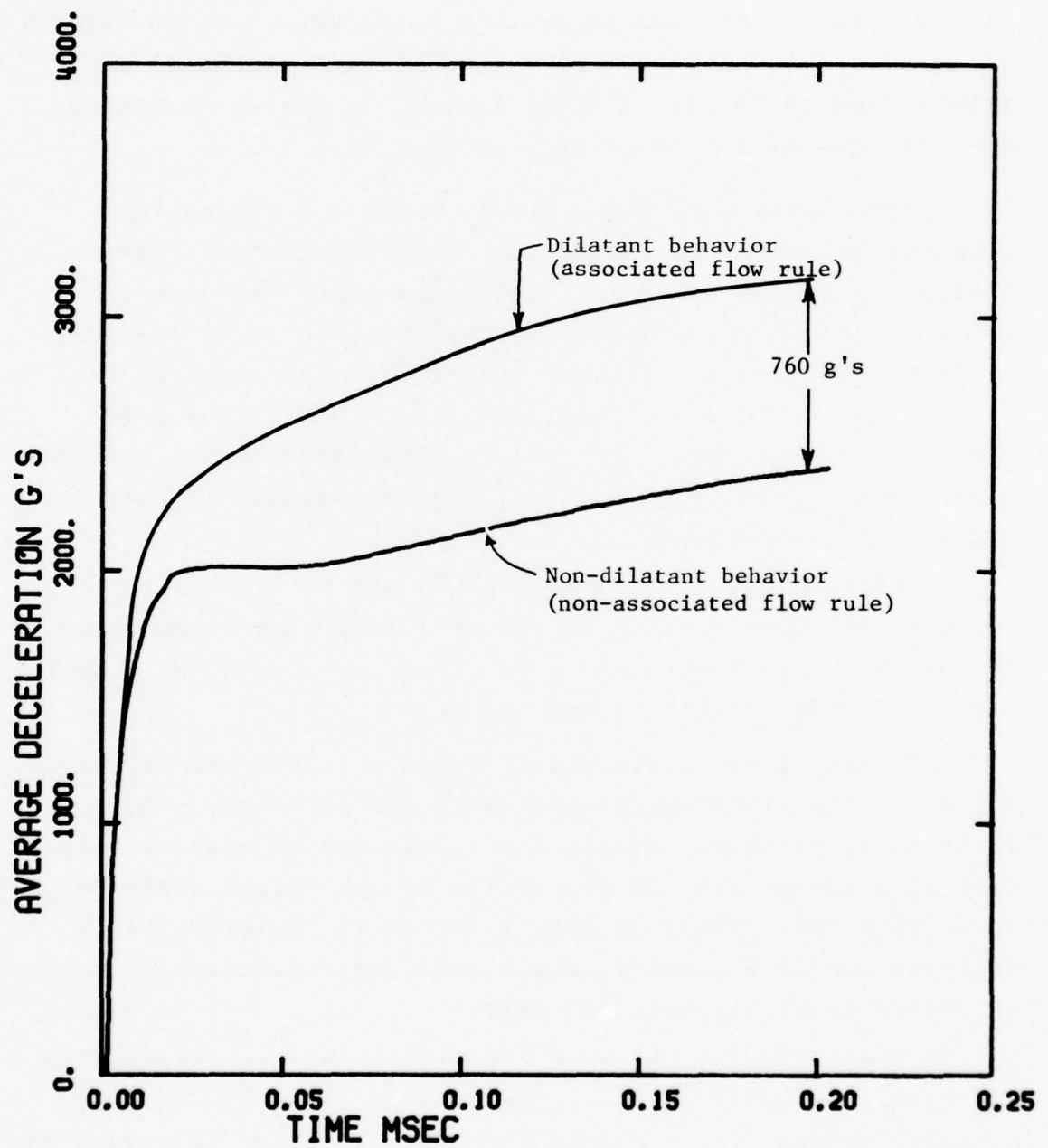in the constitutive property laboratory tests.

Figure 19. Effect of Dilatant Behavior of Target Material on Penetrator Deceleration (1500 ft/sec Impacts into Sandstone)

45

2.3.2   Stress and Force Loadings on Penetrators

Comparisons of the loading distributions on the pene-
trator nose for all the parametric cases are shown in Figures
20 to 22. All the curves give loading when the depth of
penetration is 10 in. Shading is used to denote envelopes
wherein most of the calculated values fall.

Distributions of the applied normal and tangential
stresses are shown in Figure 20. The distributions have a
similar shape, with varying amplitudes above or below the
baseline case ordered approximately the same as in the decel-
eration comparisons. All but one of the distributions fall
within the shaded area, or within about ±40% of the curve
for the baseline case. The case with doubled impact velocity
stands out, having significantly higher amplitudes, but it
retains the same shape.

Distributions of the axial force are shown in Figure 21.
The high velocity case agains shows a much higher amplitude.
The blunter nose shape case also stands out, with the distri-
bution shifted forward toward the nose tip.

Distributions of the radial force are shown in Figure 22
(data for the frictionless case were not recorded). Here, in
addition to the high velocity case, the larger size penetrator
case also stands out, in proportion to the larger surface
areas involved. (This is also a factor in the axial force
distribution in Figure 21, where the larger penetrator curve
is raised above the baseline case.)

A comparison of the peak compressive stress attained in
the target material which was originally along the axis of
symmetry (in the first column of cells) is shown in Figure 23.
The peak stress is about 6 kb for the baseline case, and
ranges between 4 and 7 kb for the various parametric cases.
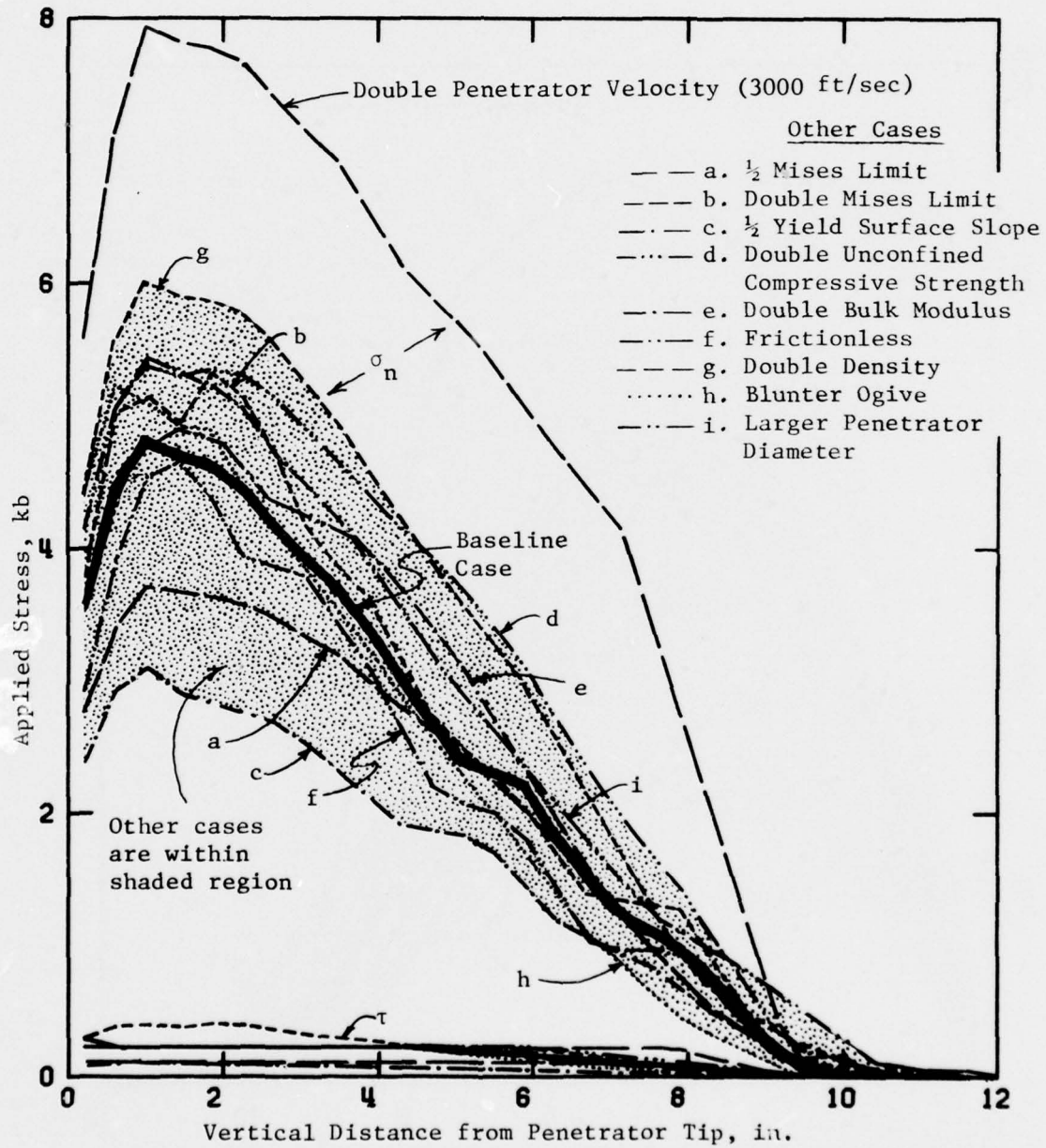The high velocity case induced peak stresses of 8-9 kb.

46

Figure 20. Comparison of Distributions of Normal and Tangential Stress (σ_n, τ) Applied to Penetrator Surface, Depth of Penetration = 10 in., Physical Parameter Study

47

Figure 21. Comparison of Distributions of Axial Force per Unit Length of the Penetrator along Penetrator Surface, Depth of Penetration = 10 in., Physical Parameter Study
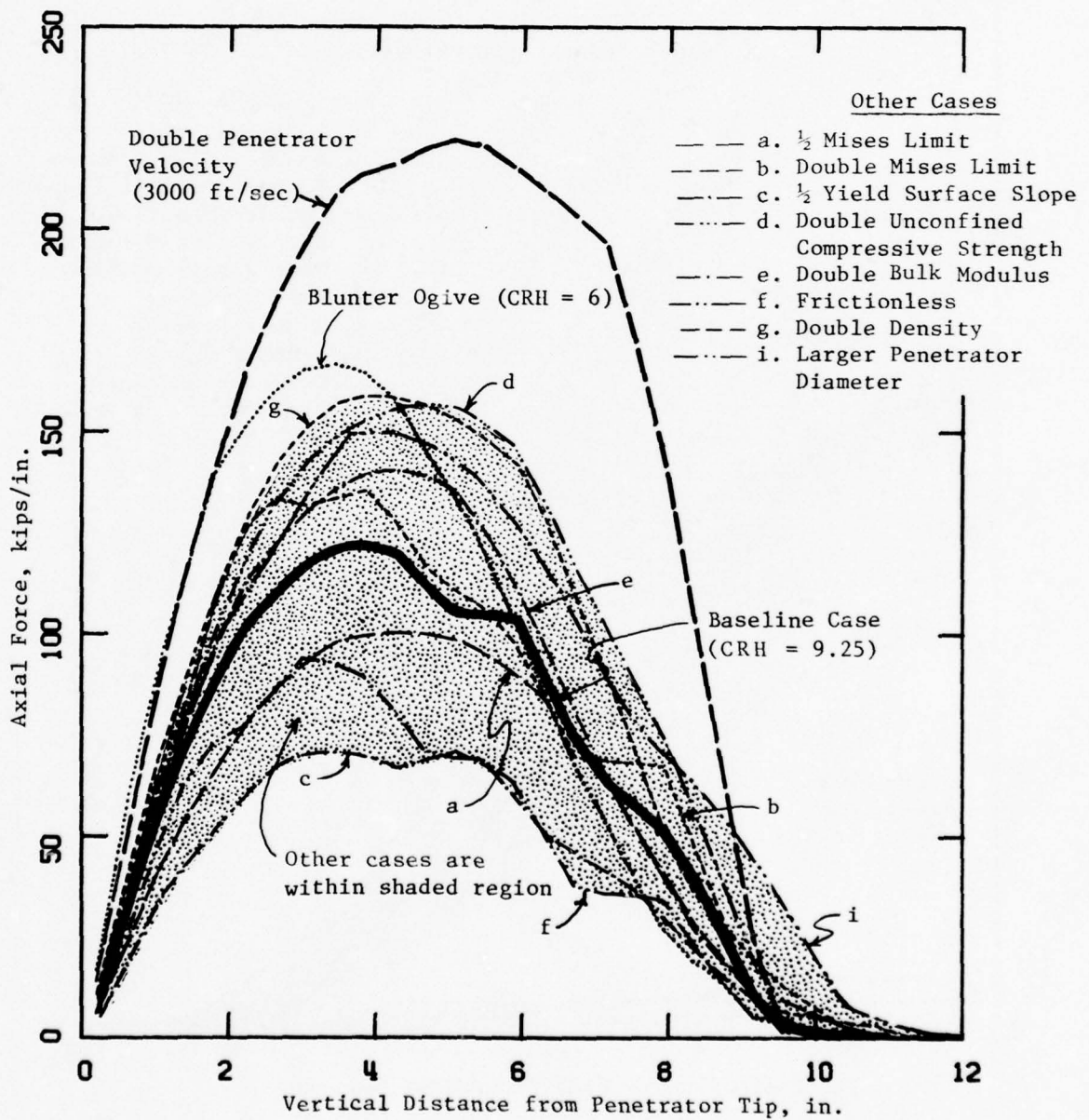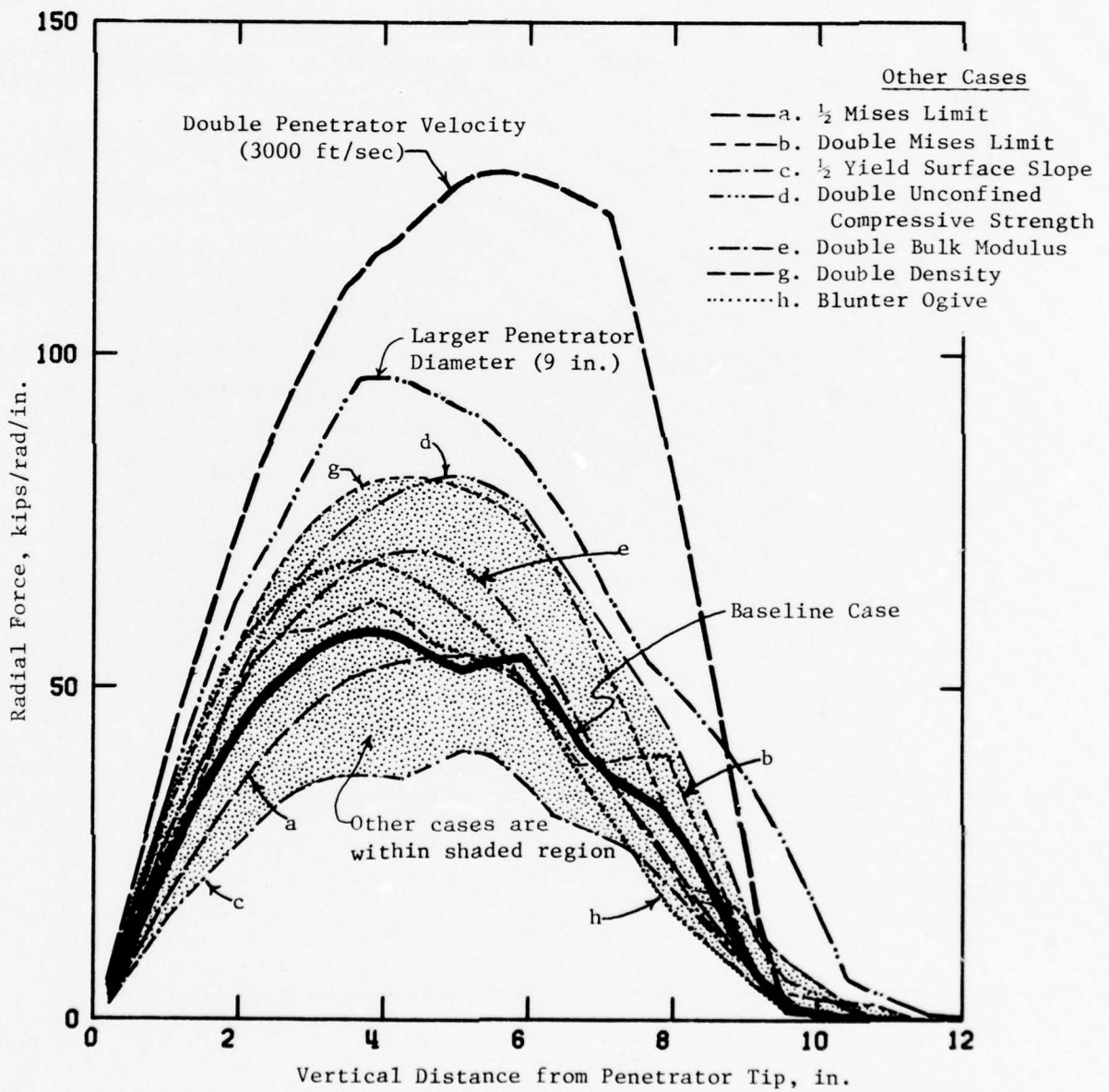
48

Figure 22. Comparison of Distributions of Radial Force per Unit Angle per Unit Length of Penetrator along Penetrator Surface, Depth of Penetration = 10 in., Physical Parameter Study
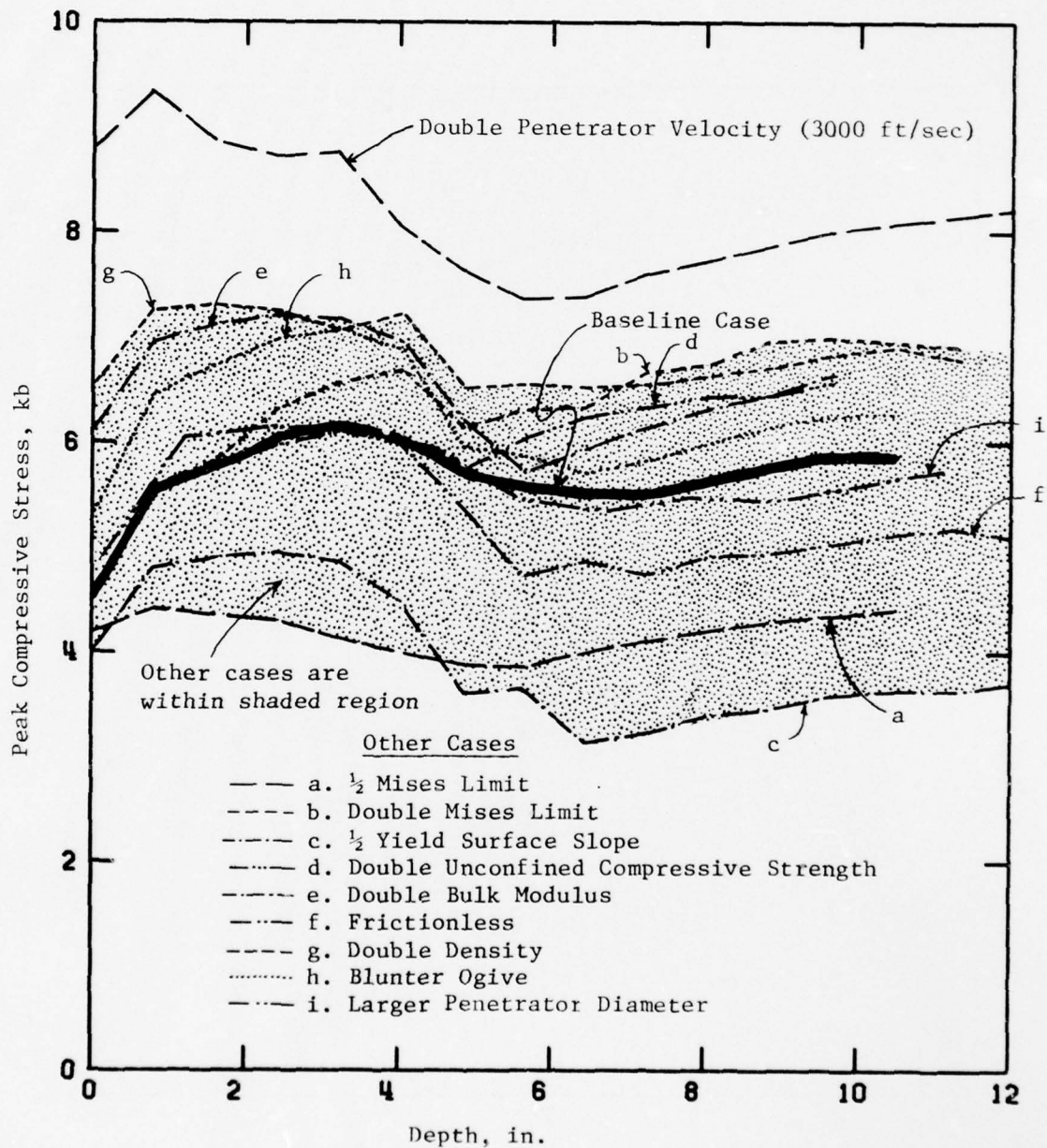
Figure 23. Comparison of Peak Compressive Stress in Target near
Axis vs Depth, Physical Parameter Study

50

2.4 Fracture Pattern Around Penetration Hole

Some additional results of the 3000 ft/sec impact case serve to illustrate an aspect of penetration in sandstone which has previously been observed in welded tuff. Figure 24 shows the fracture pattern developed in the target after penetration to a depth of 24 in. Here annular regions of totally shattered (comminuted), severely fractured, lightly fractured, and still intact material are seen at increasing radii. This pattern of fracture around penetration holes is seen in experiments in rock media.[10,11] All the material next to the penetrator and out to a maximum radius of 11 inches, is comminuted. The degraded properties of such material thus largely dominate the local processes which act on the penetrator surface (including, of course, friction).

The corresponding particle velocity field is shown in Figure 25. Diverging flow is seen around the penetrator, and ejecta near the entry hole is seen "blowing off" at about 600 ft/sec.
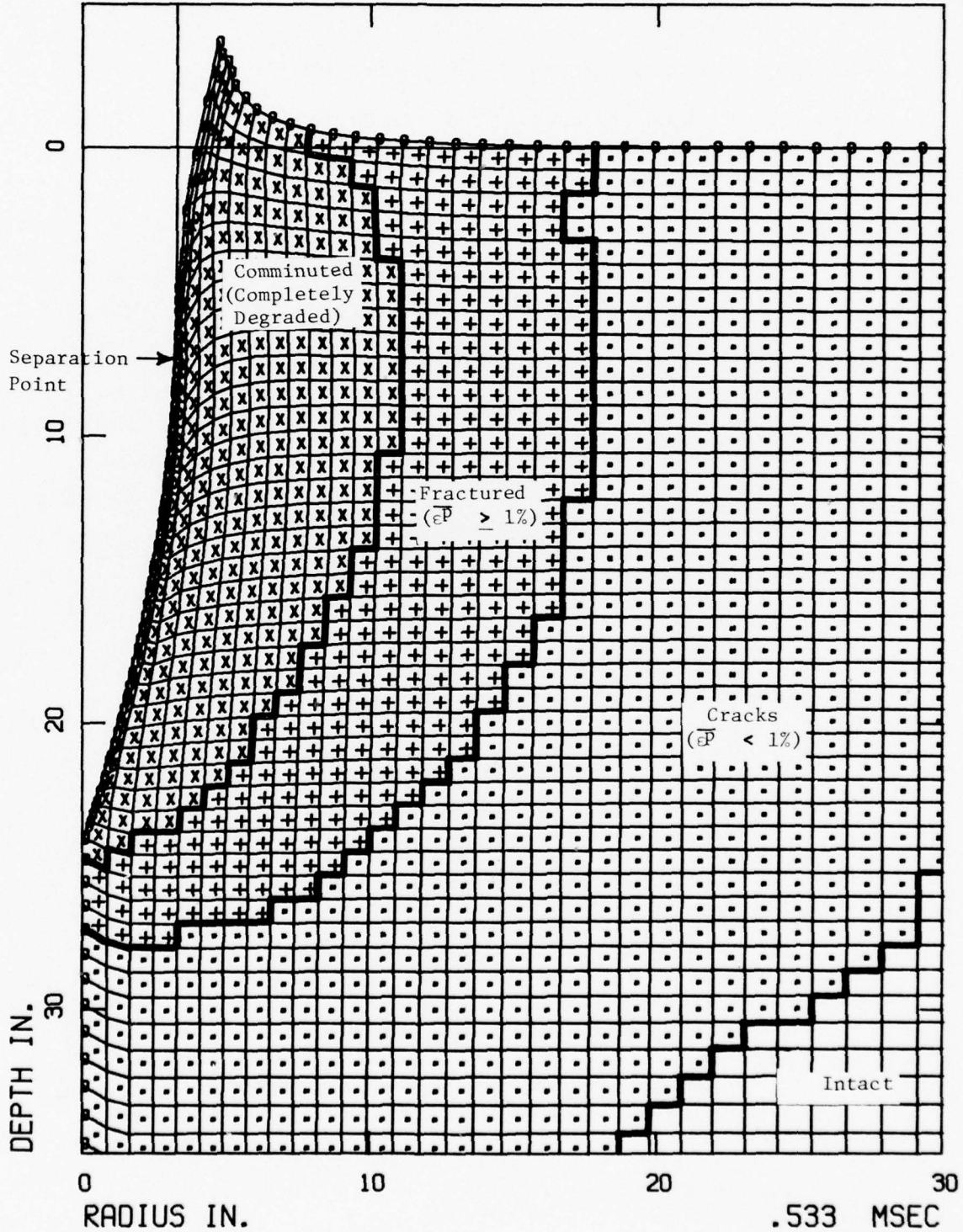
Figure 24. Lagrangian Grid and Fracture Pattern in Sandstone, Initial
Penetrator Velocity = 3000 ft/sec
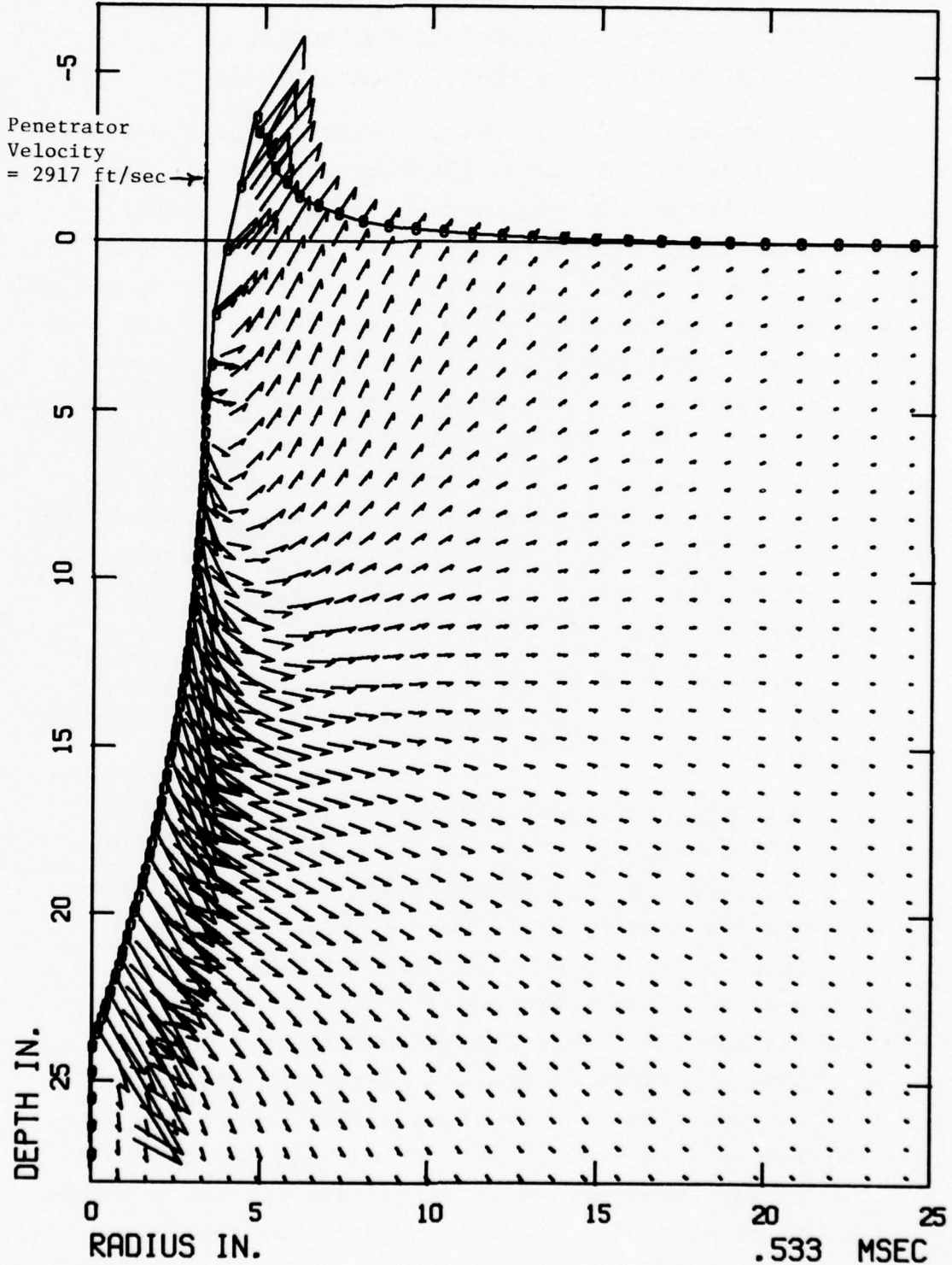
Figure 25.   Particle Velocity Field in Sandstone, Initial Penetrator
Velocity = 3000 ft/sec

53

III. EFFECTS OF COMPUTATIONAL ZONING
ON CALCULATIONS OF PENETRATION DYNAMICS

In a previous study of vehicle penetration into a soil target,[1] a large radial stress gradient was seen in the soil outward from the surface of the penetrator, particularly near the nose tip. A reasonably accurate computation of the stress field next to the penetrator is, of course, essential to determining the correct forces to be exerted on the penetrator. Where there are sharp gradients, the question of the adequacy of the spatial resolution (zone size) naturally arises. Overly coarse zoning will lead to a truncation of the gradients. As finer and finer zones are employed, the computed gradient should converge on the correct peak values. Unfortunately, there is a heavy price in computing time to be paid for fine-zoned solutions, so a compromise between accuracy and cost must be made.

Fortunately, there are several factors which tend to justify coarser zoning than at first might appear necessary. For example,

a. The region of sharp stress gradients is concentrated near the nose tip of pointed penetrators. The gradients rapidly diminish along the nose, and are usually small when the halfway station between the tip and the tangency point is reached. Since the penetrator circumference and surface area decrease sharply near the tip, an error in applied *stress* in that region produces a relatively small error in the applied *force*. (If, of course, the errors in the computations of stress are extremely large, there will be a significant error in the force applied to the penetrator.)

54

b. As will be seen, the stress gradients are
    generally much less severe for rock media, as
    compared to soil media, so zoning requirements
    are lessened for targets in rock (which are the
    primary media of interest for this program).

3.1 PENETRATOR AND TARGET CONDITIONS

The effects of zone size on numerical solution results
were examined for three different penetration problem condi-
tions, as outlined in Table 3 and Figure 26.

The basic conditions considered were the same as the
baseline conditions for the physical parameter study in
Section II. The penetrator was the DNA 400-1b, 6.5-in. dia
design, impacting at 1500 ft/sec. Three types of target
media were considered:

a. the Watching Hill layer 1 soil[1]
b. sandstone, and
c. a non-hysteretic, dilatant soft rock

The properties of these materials are listed in Table 4.

The Watching Hill layer 1 soil was modeled as a very
porous soil (air fraction = 37%). It has an extremely non-
linear loading hydrostat and is sharply hysteretic (high ratio
of unload/load moduli). It was modeled with a non-associated
flow rule and thus exhibits no dilatancy.

The sandstone model is the same as used in the physical
parameter study, except for the post failure treatment and
the friction coefficient. The sandstone has a "strong"
failure surface, with an unconfined compressive strength of
~ 6000 psi and a Mises limit of ~75,000 psi. This model can
allow tensile stresses as high as 8200 psi. Since these

55

Table 3. Penetration Problems for Zoning Study

Penetrator: 400 lb, 6.5" dia Sandia design

Impact Velocity: 1500 ft/sec

Target Medium	Density (gm/cm³)	Unconfined Compressive Strength (psi)	Response Characteristics	Projectile Nose Tip
Watching Hill Layer 1 Soil	1.49	42.6	Extremely hysteretic, non-dilatant	Beveled
Sandstone	2.0	4944	Hysteretic, dilatant	Beveled
Soft Rock	2.0	1766	Non-hysteretic, non-dilatant	Pointed

6.5" dia → ← PENETRATOR

Rigid Body
Projectile

60"

Normal Impact at 1500 ft/sec

Weight = 400 lb

W/A = 12 psi

19.5"

Nose:
CRH = 9.25
(Radius = 60.125")

Target Surface

Beveled or Pointed Nose Tip

5"
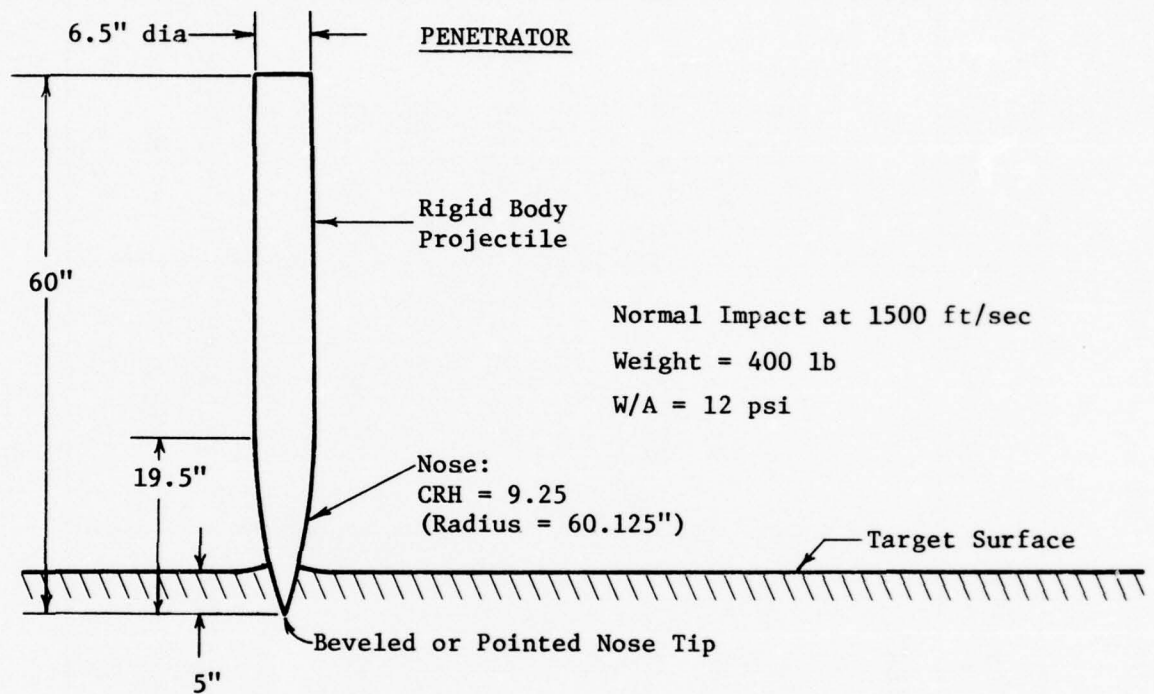
TARGET MEDIA (3 types)

a. Watching Hill Layer 1 soil
b. Sandstone
c. Soft Rock

Figure 26.   Penetration Problem Conditions for Zoning Study

TABLE 4. TARGET MEDIA PROPERTIES FOR ZONING STUDY

Property	Watching Hill Layer 1 Soil	Sandstone	Soft Rock
Density, ρ_o , gm/cm^3	1.4897	2.0	2.0
Initial value of:			
Young's modulus, E_o , psi	17,173	1,044,288	1,044,288
Shear modulus, G_o , psi	6,869	435,120	435,120
Bulk modulus, K_o , psi	11,448	580,160	580,160
Poisson's ratio, ν_o , psi	.25	.2	.2
Dilatational wave velocity, c_o , ft/sec	1,013	6,562	6,562
Unconfined compressive strength, psi	42.6	5,944	1,766
Mises limit, $Y_{max} = \sqrt{3J_2'}_{max}$, psi	750	75,365	25,122
Hydrostatic tension limit, P_{min}, psi	-12.3	-290	-72.5
Flow rule	Non-Associated	Associated	Associated
Tensile fracture model	No	Yes	No
Friction rule, $\tau = \mu \sqrt{J_{2max}'}(\sigma_n)$	$\mu = .3$	$\mu = .3$	$\mu = .3$

unrealistic tensions occur under positive (compressive) pressure, they would not be prevented by a limit on the hydrostatic tension. It was therefore decided to use a simple fracture model, in which weakened properties are assigned to a cell if the stress exceeds a critical tensile value.

The soft rock was represented by a much simpler model, to help show the impact on zoning requirements imposed by complications such as are present in the soil and sandstone models. The soft rock model has the same initial mechanical properties as sandstone, but employs a linear hydrostat, is non-hysteretic, and has a lower yield surface. Since excessive tensile stresses cannot develop with this model, no fracture model was needed. An associated flow rule was employed.

Additional description of the material models is contained in Appendix A.

The zoning study cases conducted for each of these materials are listed in Table 2 (page 17 in Section 1.3.2). For the soil and sandstone targets, the penetrator nose tip was beveled with a 45° half-angle cone, as in the DNA penetrator design. For the soft rock target, a pointed nose tip (unbeveled) was used. As in the physical parameter study, the zoning solutions were initiated with the penetrator nose-tip already buried 5-in. below the ground surface. This provides a shorter run-up time to the deceleration level for a particular impact.

The computational grid designs used for the zoning study cases employed approximately uniform cells in the vicinity of the penetrator path. The basic cell width and height in this region was a selected fraction of the projectile radius.

Zonings of 2, 4, 6, or 8 cells across a projectile radius were considered. It is useful to specify the zoning in terms of the projectile radius, since finite-difference code calculations of penetration processes scale with linear dimensions (except for gravitational or strain-rate effects or complex targets, none of which were considered here). To accommodate the pre-burial of the projectile nose, the cells next to the penetrator nose were reduced in size. However, the material in these cells was not pre-compressed; all of the target material was initially at normal density. The cells in the first two columns below the penetrator were canted upward in the initial grid. This technique, developed for previous penetration solutions, provides a more orthogonal grid as cells next to the penetrator "drag down" during the penetration process. This lengthens the time interval between rezones.

3.2 COMPARATIVE RESULTS

For the purposes of this study, the penetrator deceleration is probably the most meaningful result to use in judging the effects of zone size. Nominal deceleration levels computed for each of the zoning study cases are listed in Table 2 (page 17).

3.2.1 Soil Targets

Figure 27 gives comparative time histories of the time-averaged deceleration, $\Delta v/t$, of the penetrator in Watching Hill layer 1 soil, using zonings of 2, 4, 6, and 8 cells per projectile radius. Two-cell resolution is clearly inadequate, being insufficient to resolve the high stresses which develop directly ahead of the blunted nose tip. As a result, the penetrator decelerations are substantially lower than in the more finely-zoned runs. Based on the curves in Figure 27,
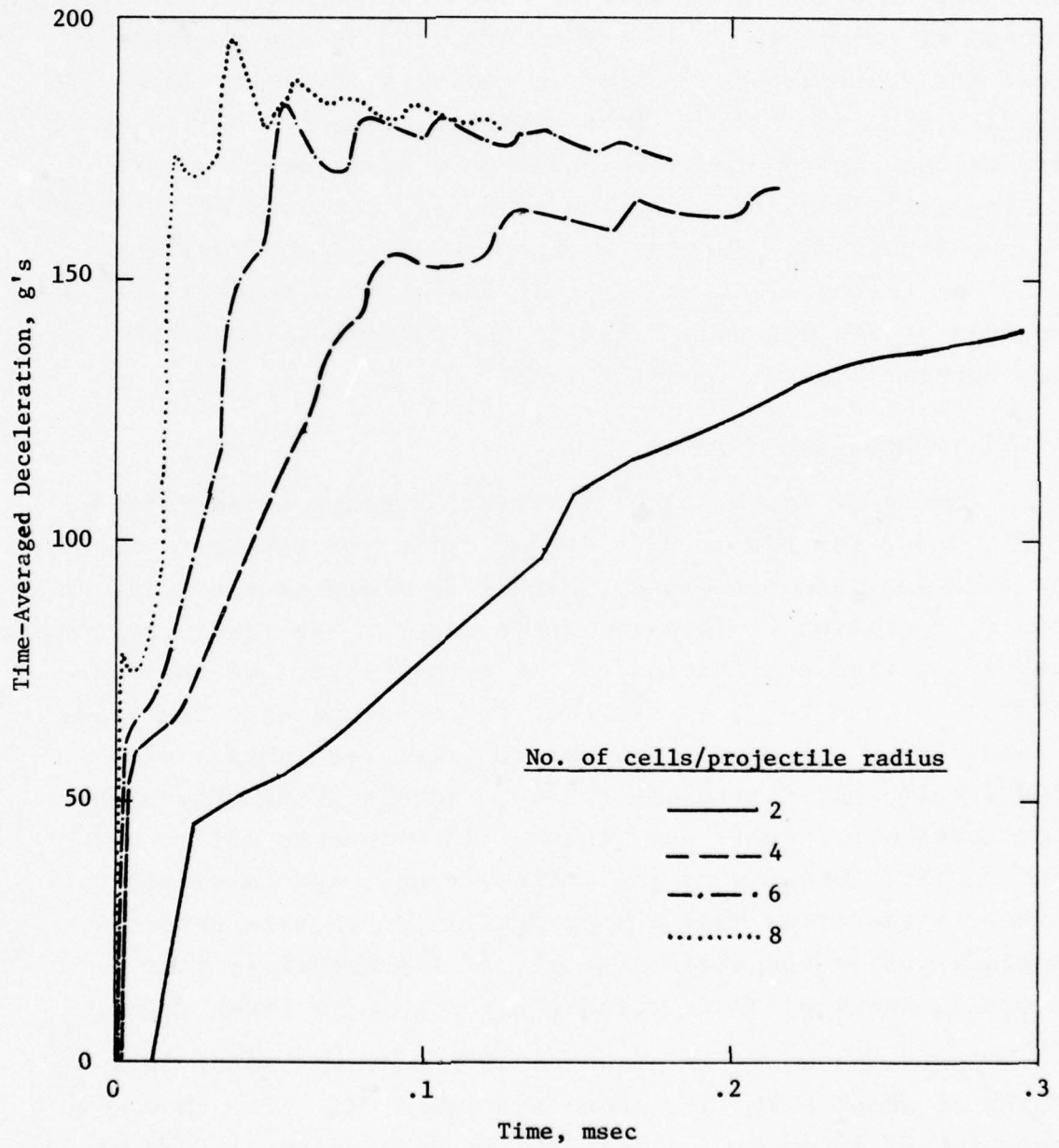
Figure 27. Effects of Zone Size on Average deceleration of Penetrator vs Time, Penetration into Soil Target

61

6 cells per penetrator radius appear to be the minimum for achieving reasonable accuracy in soil. (It should be pointed out that numerical oscillations which correspond to the frequency at which new cells are encountered by the projectile nose are a persistent problem in analyses of penetrations of blunt-tipped projectiles into material, like dry soils, which are relatively compressible and highly hysteretic. Finer zoning alleviates this problem somewhat, but does not prevent the oscillations. Further work to develop techniques for reducing the oscillations in analyses of soil penetrations is needed; it was not undertaken in the current task because of the emphasis on rock penetrations.)

3.2.2 Sandstone Targets

Figure 28 gives the histories of average acceleration, $\Delta v/t$, using zonings of 2, 4, and 6 cells per radius to analyze penetration into sandstone. Figure 29 compares the axial force and deceleration vs time for these cases. The force component resulting from application of the normal stress on the penetrator is seen to be similar for the three cases. The frictional force component is about the same for zonings of 4 and 6 cells per projectile radius, but is distinctly higher for zoning by 2 cells per radius. This inverse effect was due to the inability of the coarser-zoned case to detect fracture occurring near the projectile. Fracture causes degradation of the shear strength of the material, thus limiting the applied frictional stresses to a lower value.

Comparisons of the peak radial stress vs radius at a depth of about 6 in. are shown in Figure 30. From these results, it is concluded that zoning of 4 cells per radius is adequate. Without the complications of the fracture model, a zoning of 2-3 cells per projectile radius might be sufficient.
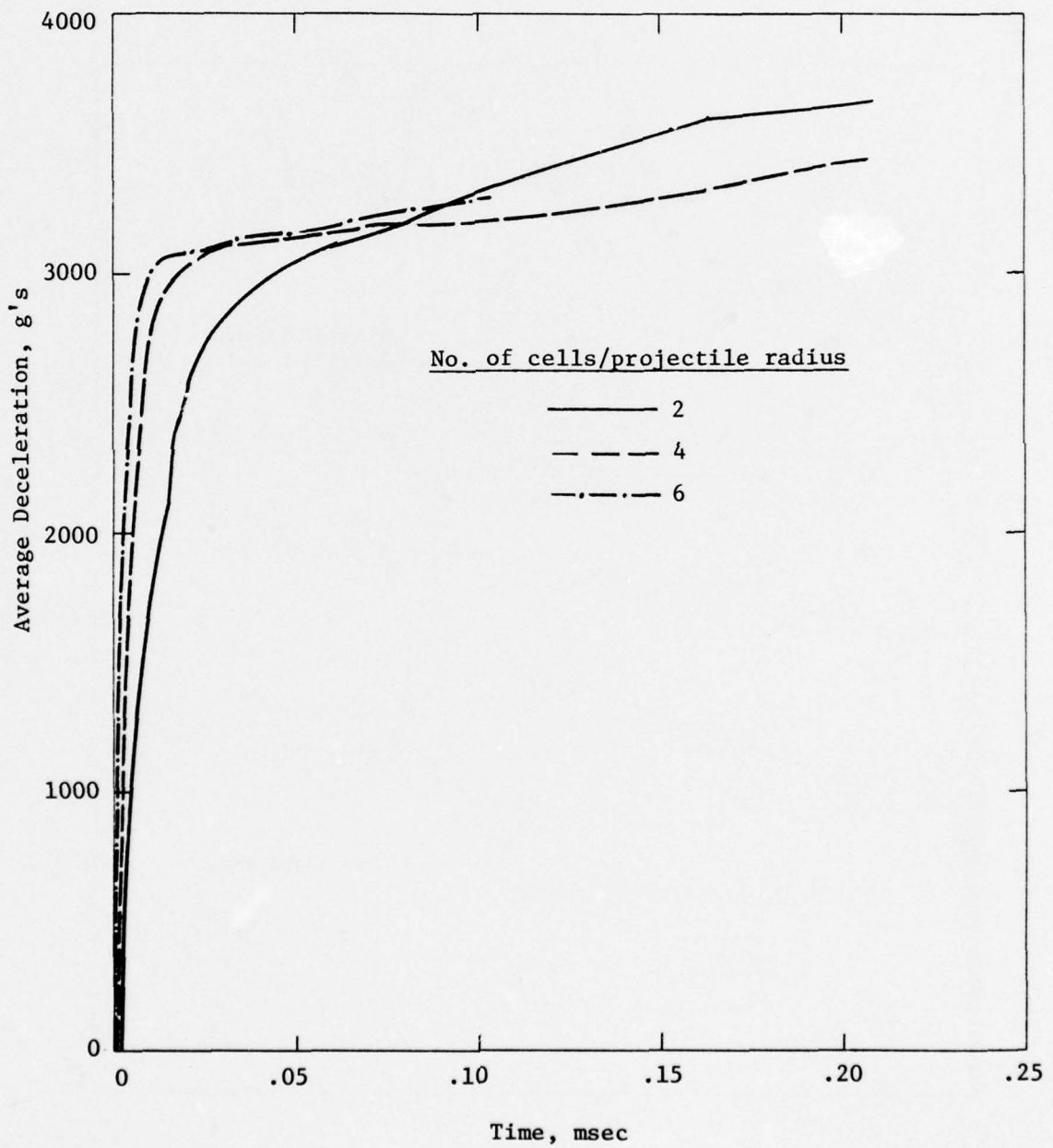
62

Figure 28. Effects of Zone Size on Average Deceleration of Penetrator vs Time, Penetration into Sandstone Target

Figure 29. Effects of Zone Size on Axial Forces on Penetrator and Deceleration of Penetrator vs Time, Penetration into Sandstone Target

64
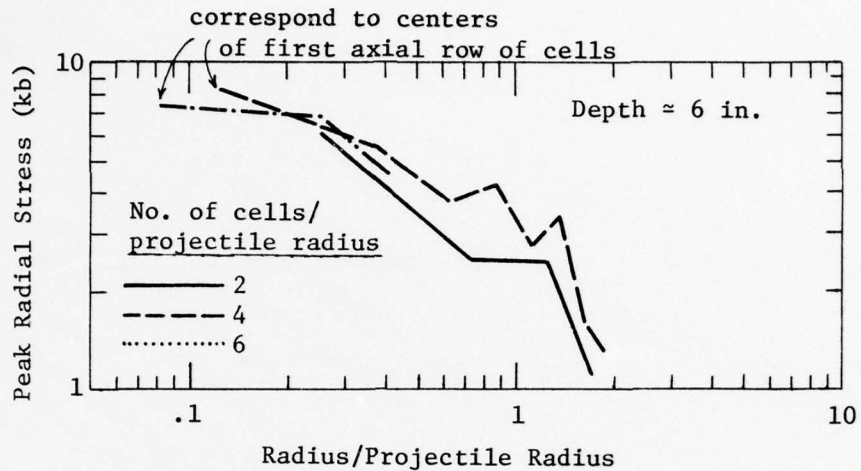
Figure 30. Effects of Zone Size on Peak Radial Stress
vs Radius, Depth ≃ 6 in., Penetration into
Sandstone

3.2.3 Soft Rock Targets

Figure 31 gives the histories of time-averaged acceleration,
$\Delta v/t$, using zonings of 4 and 6 cells per radius to analyze
penetration with a softer rock. Forces and deceleration time
histories are shown in Figure 32. Plots of peak radial stress
vs radius at a depth of about 6 in. are shown in Figure 33.

Figure 33. Effects of Zone Size on Peak Radial Stress
vs Radius, Depth ≃ 6 in., Penetration into
Soft Rock Target

65

Figure 31. Effects of Zone Size on Average Deceleration of Penetrator vs Time, Penetration into Soft Rock Target
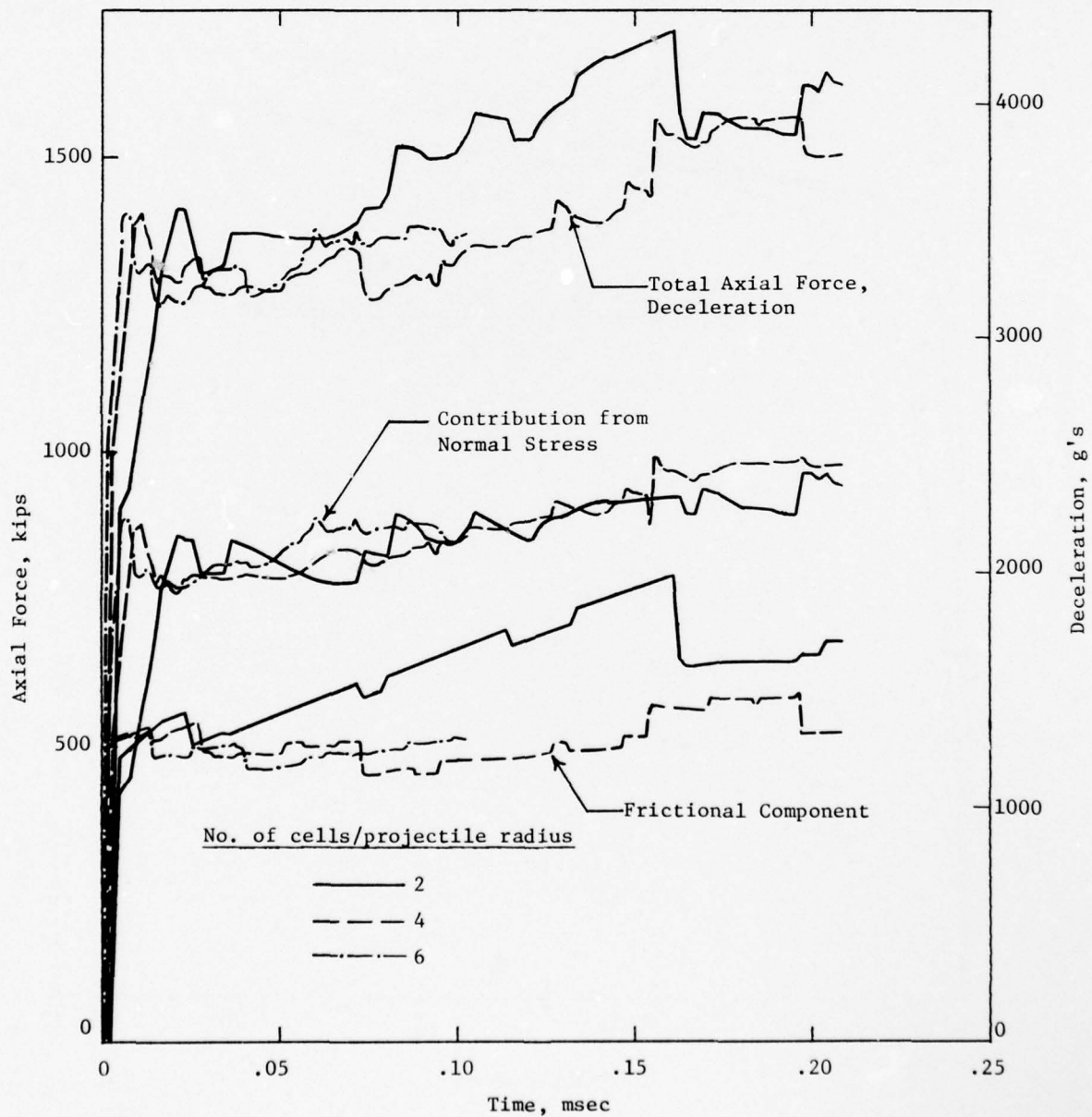
Figure 32. Effects of Zone Size on Axial Forces on Penetrator and Deceleration of Penetrator vs Time, Penetration into Soft Rock Target
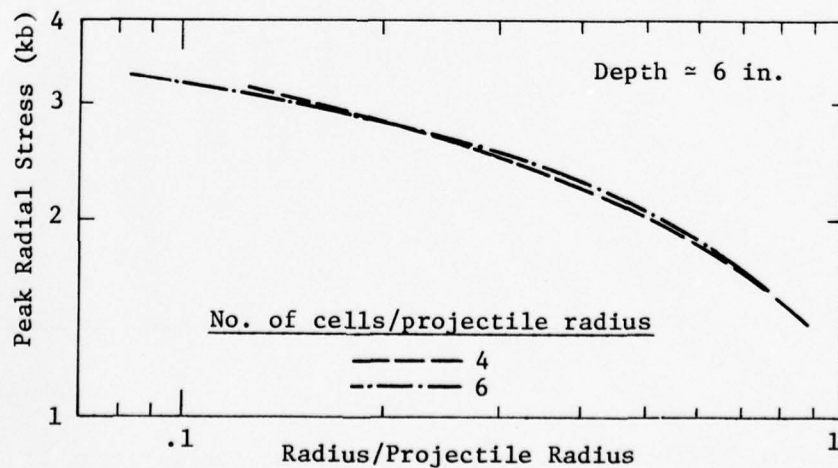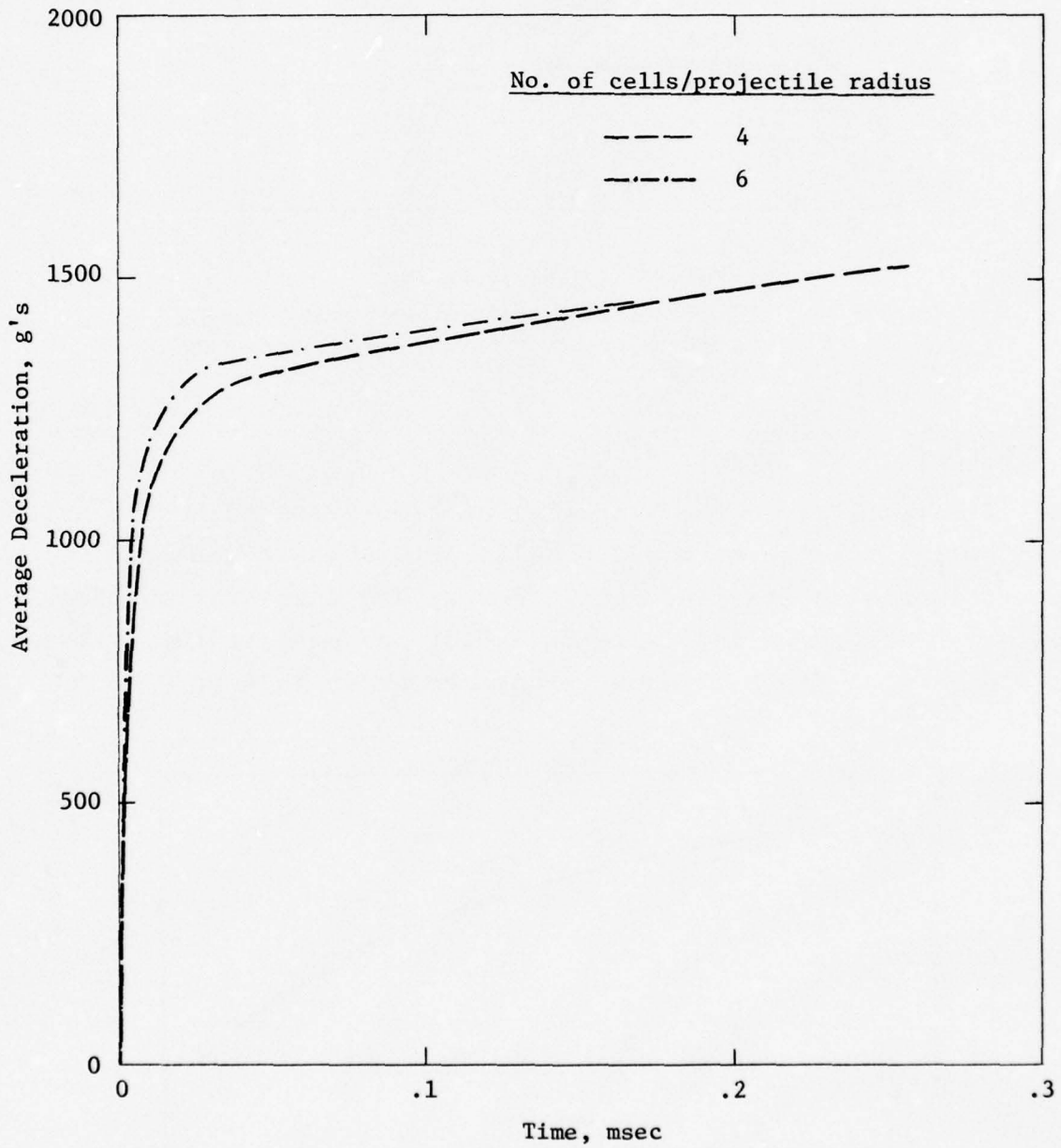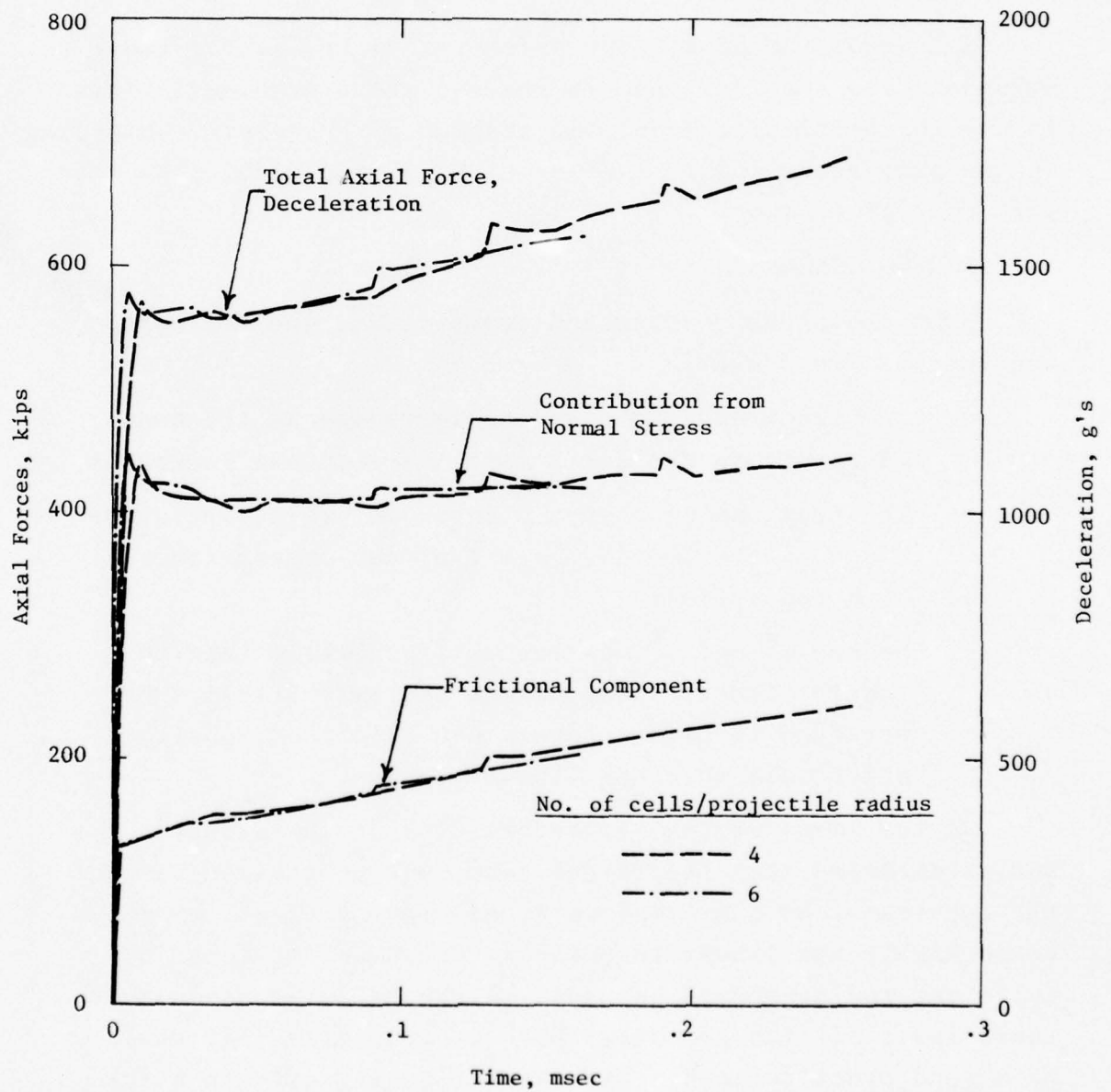
67

The closeness of the results in all these plots indicates that zoning of 4 cells per radius is certainly adequate and that an even coarser zoning might be sufficient. (Coarser zone cases were not run for this problem.)

Note that the penetrator deceleration traces for these solutions are smoother than in the sandstone problems. This is due to the simpler model and absence of hysteretic unloading in the soft rock, and to the use of a pointed nosetip on the soft rock penetrator.

3.3 ZONING CONCLUSIONS

From the above results and comparisons, the following conclusions are drawn:

a. The required zone fineness increases as the non-linearity in the earth material response increases.

b. The presence of abrupt changes in projectile shape (such as the beveled nose tip) may impose finer zone requirements.

c. Higher impact velocities will generally tend to require finer zoning, since the material will be stressed to higher levels and will thus usually enter into more non-linear regimes.

On the basis of the limited results of this study, we would recommend that the target zone size in the vicinity of the penetrator be a minimum of 4 cells per projectile radius. Where highly non-linear response is expected, at least 6 cells per radius should be used. Since it is impossible to investigate all the potential problem conditions, it would be a good practice to briefly examine zoning effects before computing new penetration problems which involve substantial changes in material properties, nose geometries, or impact velocity.

IV. COMMENTS

The results of this study are mostly favorable to the technology and development of earth penetrating weapons, for the following reasons:

a. For a given type target medium (soil, soft rock, hard rock), lack of detailed property information for potential target materials and natural variations in target properties should not introduce large uncertainties in penetrator performance. *Generally, the percentage uncertainty in penetration dynamics will be less than the percentage uncertainty in target media properties.* In the parametric study, factor of two changes in basic target properties led to changes in penetrator decelerations of 5 to 50%.

b. The most critical target properties are the strength and frictional characteristics of the material next to the penetrator; for penetrations into rock, this material is severely fractured. It thus becomes important to ascertain the *post-fracture* properties of rock. Efforts to improve knowledge of constitutive properties and penetration processes should emphasize this area. Probably the greatest uncertainty in predicting penetrator dynamics is the frictional force applied to the penetrator.

c. Impact and design parameters were not examined in detail in this study. It is nonetheless evident, for a given type target medium, that *the impact conditions and penetrator design are generally more important factors in penetration dynamics than the detailed constitutive properties of the target medium.* Fortunately, from the standpoint of design analyses, the impact and design parameters are generally specified, thereby minimizing any uncertainties. The impact velocity clearly has a primary effect on penetrator dynamics.

69

Unfortunately, there is probably no simple universal functional
relationship between rigid body deceleration and impact vel-
ocity; rather, the relationship depends on the target medium
and the velocity regime, and probably on penetrator shape
as well.

Additional study is needed in order to provide a basis
for optimizing nose shape for different types of earth pene-
trators. Designers need information with which to select
nose shapes which give the appropriate balance of peak accel-
eration, penetrating capability, and ability to perform in
oblique and yawed impacts.

REFERENCES

1. M. H. Wagner, K. N. Kreyenhagen, and W. S. Goerke, *Numerical Analysis of DNA Earth Penetrator Experiment at DRES,* Defense Nuclear Agency, Report DNA 3537F, 18 June 1975.

2. Y. M. Ito, K. N. Kreyenhagen, and M. H. Wagner, *Internal Response Analyses of Earth Penetrators,* Defense Nuclear Agency, Report DNA 4118T, August 1976.

3. M. H. Wagner, C. C. Fulton, and K. N. Kreyenhagen, *Finite-Difference Code Analyses of Earth Penetrator Dynamics in Rock Media,* Defense Nuclear Agency, Report DNA 4069T, November 1976.

4. Y. M. Ito, M. H. Wagner, and K. N. Kreyenhagen, *SBM Penetrator: Phase I Penetration and Response Design Analysis, Summary of Results,* California Research and Technology, August 1976.

5. M. H. Wagner, C. C. Fulton, and W. S. Goerke, *Calculation of Reverse Ballistic Test into Dakota Sandstone at 1800 ft/sec, Data Package,* California Research and Technology, February 1976.

6. M. H. Wagner, K. N. Kreyenhagen, and W. S. Goerke, *Numerical Analysis of Projectile Impact and Deep Penetration into Earth Media,* U. S. Army Engineer Waterways Experiment Station, Report S-75-4, August 1975.

7. W. J. Patterson, *DNA/Sandia Soil Penetration Experiment at DRES: Results and Analysis,* Defense Nuclear Agency, Report SAND 75-0001, 16 October 1975.

8. Y. M. Ito, K. N. Kreyenhagen, G. E. Eggum, and W. S. Goerke, *Analysis of Dynamic Stresses within a Terminal Delivery Vehicle during Penetration of a Hard Earth Target,* U. S. Army Engineer Waterways Experiment Station, Report S-75-1, February 1975.

9. P. F. Hadala, *Visit to Tonopah Test Range, 14-15 July 1975,* U. S. Army Engineer Waterways Experiment Station, Memorandum for Record, 13 August 1975.

REFERENCES (Cont'd)

10. W. J. Patterson, *Projectile Penetration of In Situ Rock*, Sandia Laboratories, Report SLA-73-0831, November 1973.

11. P. F. Hadala, *Tentative Plan for Constitutive Property Testing at the Mount Helen Site, Tonopah Test Range, Nevada*, U. S. Army Engineer Waterways Experiment Station, Memorandum for Record, 4 December 1974.

APPENDIX A

MATERIAL MODELS FOR ZONING STUDY

A.1 WATCHING HILL LAYER 1 SOIL

The material model used for the soil was the same as
that used in the previous calculation of the DNA penetrator
experiment at DRES, as described in Reference 1. One change
was made with respect to the friction rule used to compute
the applied shear stress on the penetrator surface: the
coefficient in the friction equation was changed to 0.3;
i.e.,

$$\tau = 0.3 \frac{Y(\sigma_n)}{\sqrt{3}}$$

from the 0.6 value used previously. The 0.3 value was also
used for the sandstone and soft rock cases.

A.2 SANDSTONE

A hysteretic elastic-ideally plastic model, using an
associated flow rule and a simple fracture criterion, was
formulated to represent typical properties and behavior of
sandstone. The model was not intended to represent the rock
at a specific site. The model was formulated such that the
mechanical properties in loading and unloading depend on the
current elastic volumetric strain (μ) and the maximum loading
state (P_{max}, μ_{max}) which the material has experienced.

Symbol Definitions

B = bulk modulus

G = shear modulus

J_2' = second invariant of deviatoric stresses

P = pressure (mean normal stress)

P_{max} = maximum pressure reached by a material element

$\mu = \dfrac{\rho^e}{\rho_o} - 1$ = natural volumetric strain (elastic)

μ_{max} = maximum volumetric strain (elastic) reached by a material element

ν_ℓ = Poisson's ratio in loading

ν_u = Poisson's ratio in unloading, reloading

ρ^e = density (elastic)

ρ_o = normal density

Loading Hydrostat

$$P = K_m \mu - (K_m - K_o) \mu^* \left[1 - \exp^{-\frac{\mu}{\mu^*}} \right]$$

Unloading Hydrostat $(\mu < \mu_{max})$

$$P = K_o'(\mu - \mu_s) \qquad\qquad \mu \leq \mu_s$$

$$P = K_o'(\mu - \mu_s) + A(\mu - \mu_s)^\alpha \qquad\qquad \mu > \mu_s$$

where

$$A = \frac{P_{max} - K_o'(\mu_{max} - \mu_s)}{(\mu_{max} - \mu_s)^\alpha}$$

$$\alpha = \frac{(\mu_{max} - \mu_s)(K_m' - K_o')}{P_{max} - K_o'(\mu_{max} - \mu_s)}$$

74

and
$$K_o' = f(\mu_s)$$

$$K_m' = K_m - (K_m - K_{uo}) \exp \frac{-\mu_{max}}{\mu_u^*}$$

$$\mu_s = g(\mu_{max})$$

In this model, $f(\mu_s)$ is constant and

$$g(\mu_{max}) = \text{Min}(a\mu_{max}, \mu_c)$$

The values of the constants are:

a	= .6	μ_c	= .25
$f(\mu_s)$	= const = 50 kb	μ^*	= 1.5
K_o	= 40 kb	μ_u^*	= 1.5
K_m	= 800 kb	ρ_o	= 2 gm/cm^3
K_{uo}	= 150 kb		

Hydrostatic tension was limited by imposing a minimum value of pressure: P_{min} = -.02 kb.

Shear Modulus
$$G = \text{Min} \left[\frac{3B(1-2\nu)}{2(1+\nu)} , G_{max} \right]$$

where

$$B = (\mu+1)\frac{dP}{d\mu}$$

For loading, a constant Poisson's ratio, ν_ℓ = .2, was used and for unloading, a constant Poisson's ratio, ν_u = .18, was used, except that a limit on the resulting shear modulus of G_{max} = 200 kb was imposed.

75

Yield Surface and Fracture Model

The yield surface defines the limit of elastic states. For tentative stress states lying outside the yield surface, plastic flow is computed in accordance with the associated flow rule.

The yield surface used for intact sandstone was:

$$\sqrt{J'_{2_{max}}} = \text{Min } (k_1 + k_2 P, \ k_3)$$

where $k_1 = .1$ kb, $k_2 = 1.0$, $k_3 = 3$ kb

The following tensile fracture model was used to prevent the buildup of large tensile stresses.* For material in a cell which develops a principal stress exceeding a critical tensile stress, the material is considered to have fractured and is thereafter assigned degraded material properties. The critical tensile stress was set at 20 bars and the fractured material was assigned a lowered failure surface, defined by:

$$k_1 = 0 \qquad\qquad k_2 = .5 \qquad\qquad k_3 = 1.5 \text{ kb}$$

The failure surfaces for the intact and fractured material are shown in Figure A-1. In addition, the fractured material was modeled as a constant shear modulus material, with $G = 15$ kb, and P_{min} was set to zero.

Model Results

Plots of vertical stress vs vertical strain, stress difference vs pressure, and pressure vs volumetric strain for

---

* The more complex model for fracture/post-fracture behavior in the sandstone used in the physical parameter study is described in Section 2.1.

76

uniaxial strain load-unload paths computed with the model
are shown in Figures A-2 to A-4. The points where fracture
occurs upon unloading are shown by x's on Figures A-3 and A-4.

Friction Rule

The following friction rule was used to compute the
shear stress τ acting at the penetrator/rock interface:

$$\tau = .3 \sqrt{J'_{2max}(\sigma_n)}$$

Here σ_n, the stress component normal to the penetrator sur-
face, is the argument of the yield surface function, $\sqrt{J'_{2max}}$.

A.3 SOFT ROCK

Loading and Unloading Hydrostat (Non-Hysteretic)

$$P = -K\left(\frac{1}{\eta} - 1\right)$$

A constant shear modulus model was employed, with $G = 30$ kb.

Yield Surface (Associated Flow Rule)

$$\sqrt{J'_2} = \text{Min} \ (k_1 + k_2 P, \ k_3)$$

The values of the constants are:

$\rho_o = 2. \ \text{gm/cm}^3$ $k_2 = .5$

$K = 40$ kb $k_3 = 1$ kb

$k_1 = .05$ kb $P_{min} = -.005$ kb

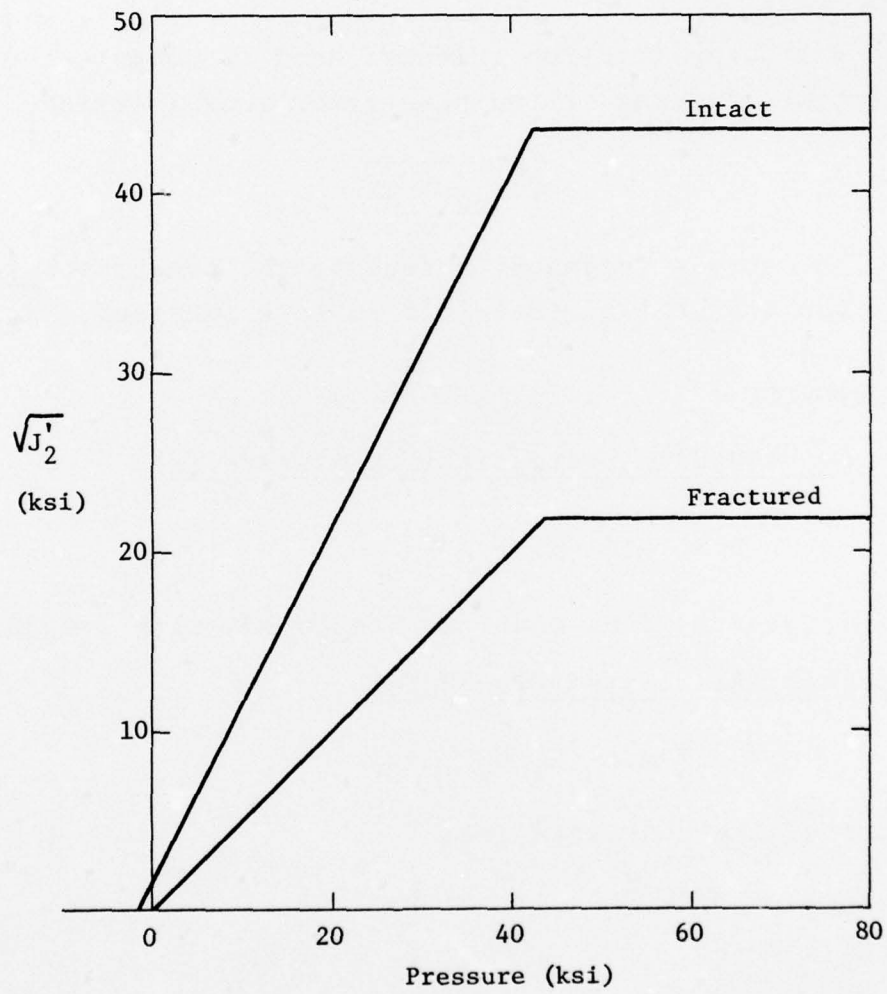The yield surface for this model is shown in Figure A-5.

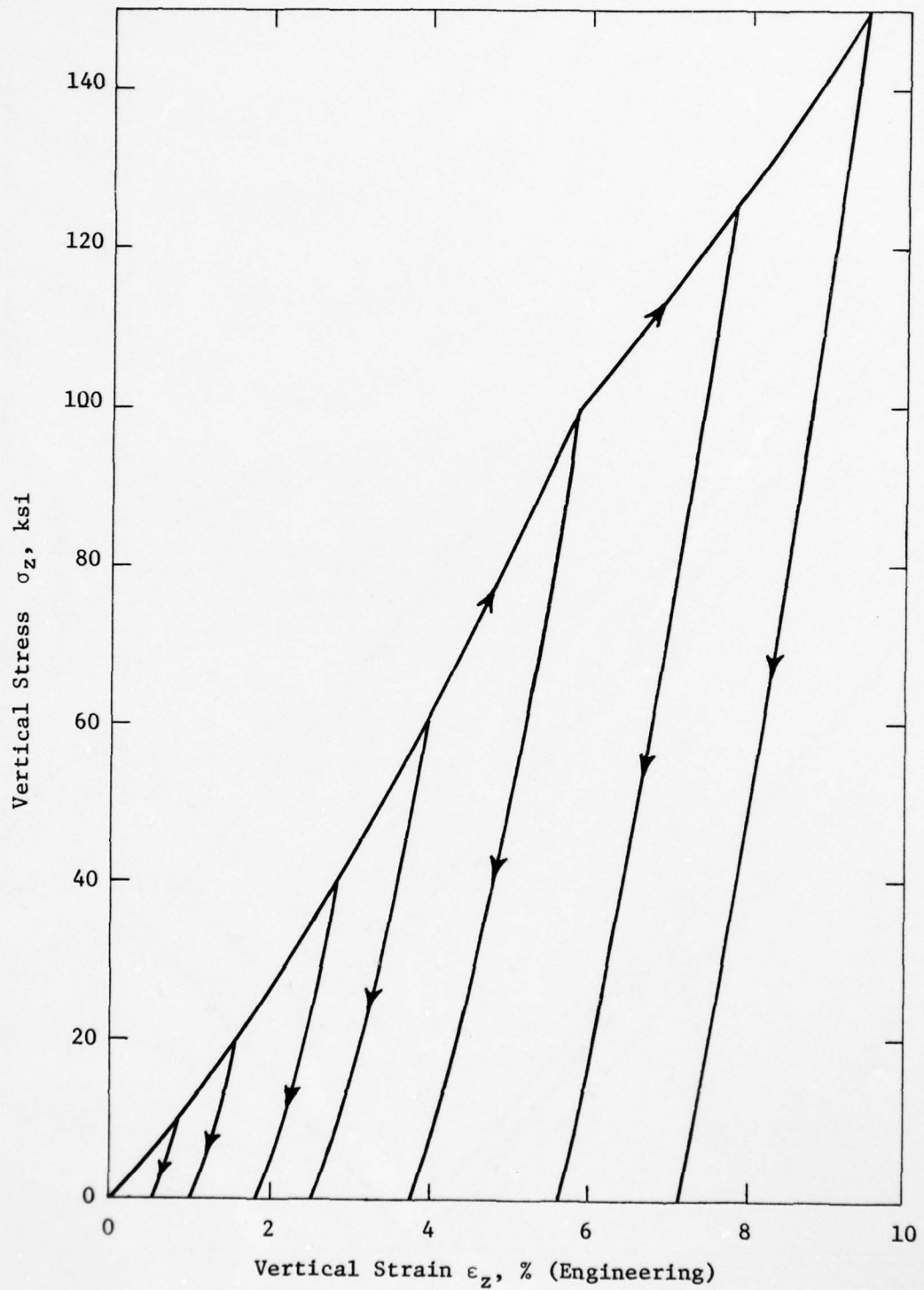Figure A-1. Failure Surfaces for Intact and Fractured Sandstone

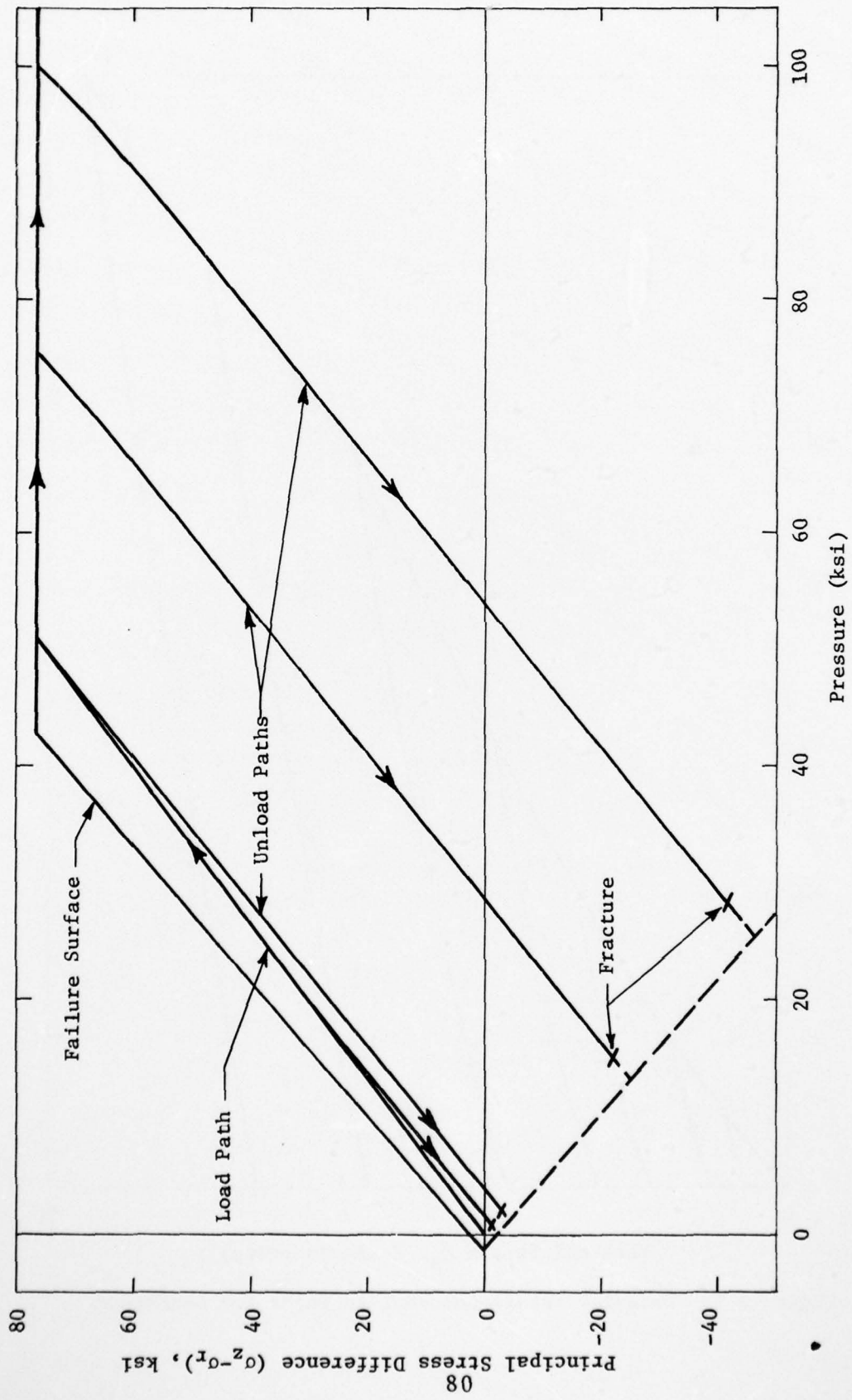Figure A-2. Uniaxial Strain Load-Unload Paths for Sandstone

Figure A-3. Uniaxial Strain Stress Paths and Failure Surface for Sandstone
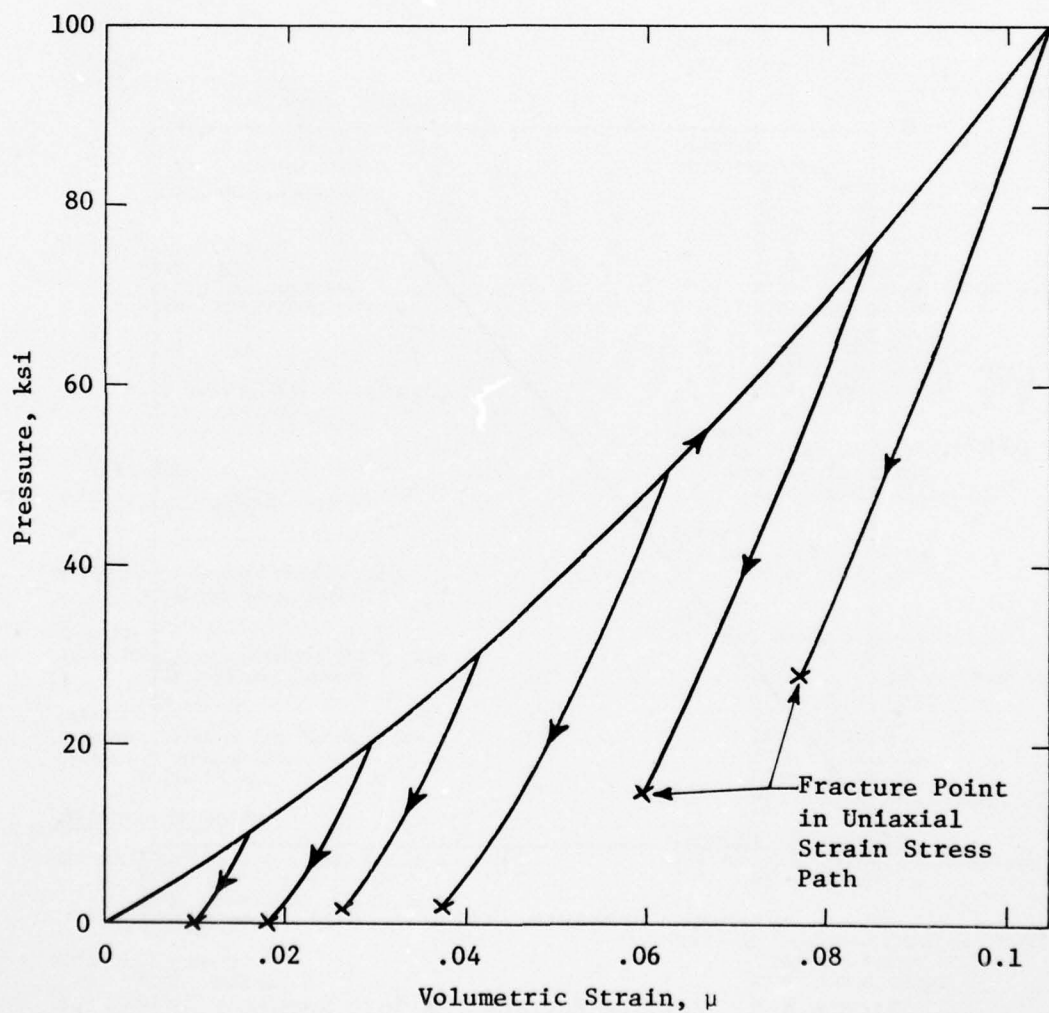
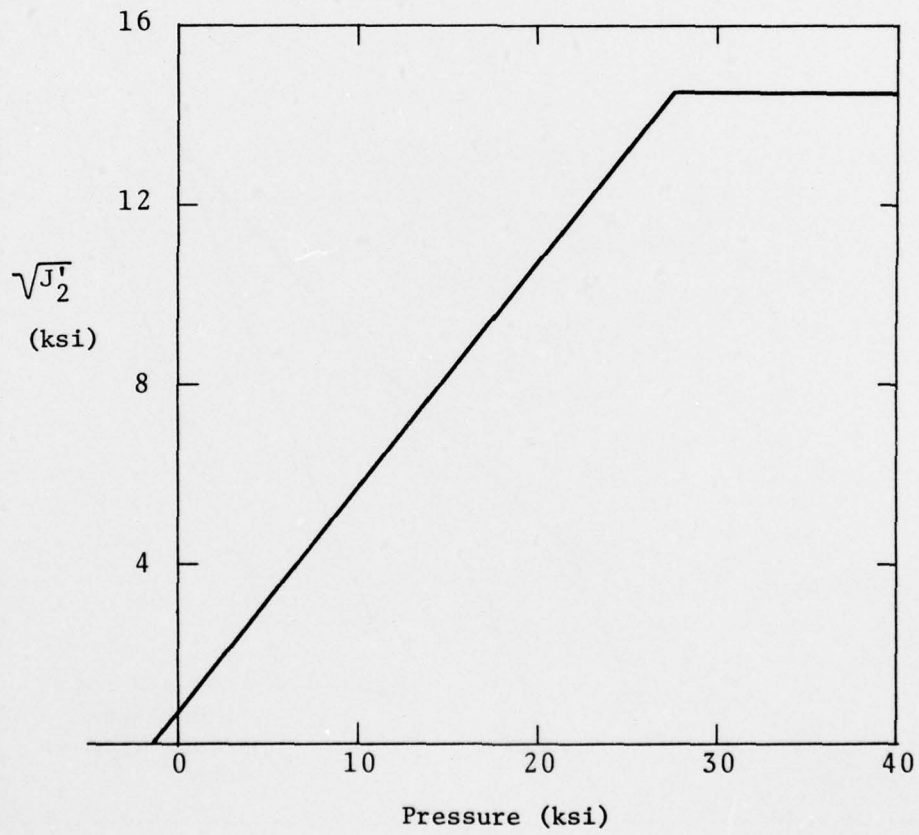Figure A-4. Uniaxial Strain Load-Unload Paths in P-μ Space for Sandstone

81

Figure A-5. Failure Surface for Soft Rock

DISTRIBUTION LIST

DEPARTMENT OF DEFENSE

Director
Defense Advanced Rsch. Proj. Agency
      ATTN: Technical Library

Director
Defense Civil Preparedness Agency
Assistant Director for Research
      ATTN: Admin. Officer

Defense Documentation Center
Cameron Station
12 cy ATTN: TC

Director
Defense Intelligence Agency
      ATTN: DB-4C, Edward O'Farrell
      ATTN: Charles A. Fowler
      ATTN: DT-2, Wpns. & Sys. Div.
      ATTN: Technical Library
      ATTN: DI-7E

Director
Defense Nuclear AGency
      ATTN: DDST
      ATTN: TISI, Archives
3 cy   ATTN: TITL, Tech. Library
5 cy   ATTN: SPSS
      ATTN: SPAS

Director of Defense Rsch. & Engineers
      ATTN: S&SS(OS)

Commander
Field Command
Defense Nuclear Agency
      ATTN: FCPR

Director
Interservice Nuclear Weapons School
      ATTN: Document Control

Director
Joint Strat. Tgt. Planning Staff, JCS
      ATTN: STINFO, Library

Chief
Livermore Division Fld. Command, DNA
Lawrence Livermore Laboratory
      ATTN: FCPRL

DEPARTMENT OF THE ARMY

Dep. Chief of Staff for Rsch. Dev. & Acq.
      ATTN: Technical Library
      ATTN: DAMA-CSM-N, LTC G. Ogden
      ATTN: DAMA(CS), MAJ A. Gleim

Chief of Engineers
2 cy   ATTN: DAEN-MCE-D
2 cy   ATTN: DAEN-RDM

Deputy Chief of Staff for Ops. & Plans
      ATTN: Dir. of Chem. & Nuc. Ops.
      ATTN: Technical Library

DEPARTMENT OF THE ARMY (Continued)

Chief
Engineer Strategic Studies Group
      ATTN: DAEN-FES

Commander
Frankford Arsenal
      ATTN: L. Baldini

Project Manager
Gator Mine Program
      ATTN: E. J. Linddsey

Commander
Harry Diamond Laboratories
      ATTN: DRXDO-RBH, James H. Gwaltney
      ATTN: DRXDO-NP

Commander
Picatinny Arsenal
      ATTN: Technical Library
      ATTN: P. Angelloti
      ATTN: Paul Harris
      ATTN: Ernie Zimpo
      ATTN: Marty Margolin
      ATTN: β. Shulman, DR-DAR-L-C-FA
      ATTN: Ray Moesner
      ATTN: Jerry Pental
      ATTN: SMUPA-AD-D-A-7
      ATTN: SMUPA-AD-D-A
      ATTN: SMUPA-AD-D-M

Commander
Redstone Scientific Information Ctr.
U.S. Army Missile Command
      ATTN: Chief, Documents

Commander
U.S. Army Armament Command
      ATTN: Tech. Lib.

Director
U.S. Army Ballistic Research Labs.
      ATTN: G. Grabarek
      ATTN: J. H. Keefer, DRDAR-BLE
      ATTN: J. W. Apgar
      ATTN: DRXBR-TB
      ATTN: DRXBR-X
      ATTN: G. Roecker
      ATTN: A. Ricchiazzi
2 cy   ATTN: Tech. Lib., Edward Baicy

Commander and Director
U.S. Army Cold Region Res. Engr. Lab.
      ATTN: G. Swinzow

Commander
U.S. Army Comb. Arms Combat Dev. Acty.
      ATTN: LTC Pullen
      ATTN: LTC G. Steger

Commander
U.S. Army Engineer Center
      ATTN: ATSEN-SY-L

DEPARTMENT OF THE ARMY (Continued)

Division Engineer
U.S. Army Engineer Div., Huntsville
    ATTN: HNDED-SR

Division Engineer
U.S. Army Engineer Div., Missouri Rvr.
    ATTN: Tech. Library

Commandant
U.S. Army Engineer School
    ATTN: ATSE-TEA-AD
    ATTN: ATSE-CTD-CS

Director
U.S. Army Engr. Waterways Exper. Sta.
    ATTN: William Flathau
    ATTN: Guy Jackson
    ATTN: D. K. Butler
    ATTN: Technical Library
    ATTN: John N. Strange
    ATTN: P. Hadala
    ATTN: Leo Ingram
    ATTN: Behzad Rohani

Commander
U.S. Army Mat. & Mechanics Rsch. Ctr.
    ATTN: Technical Library

Commander
U.S. Army Materiel Dev. & Readiness Cmd.
    ATTN: Technical Library

Director
U.S. Army Materiel Sys. Analysis Acty.
    ATTN: Joseph Sperazza

Commander
U.S. Army Missile Command
    ATTN: W. Jann
    ATTN: F. Fleming
    ATTN: J. Hogan

Commander
U.S. Army Mobility Equip. R&D Ctr.
    ATTN: Technical Library
    ATTN: STSFB-XS
    ATTN: STSFB-MW

Commander
U.S. Army Nuclear Agency
    ATTN: Doc. Control
    ATTN: Tech. Library

Commander
U.S. Army Training and Doctrine Comd.
    ATTN: LTC J. Foss
    ATTN: LTC Auveduti, COL Enger

Commandant
U.S. Army War College
    ATTN: Library

U.S. Army Mat. Cmd. Proj. Mngr. for Nuc. Munitions
    ATTN: DRCPM-NUC

DEPARTMENT OF THE NAVY

Chief of Naval Operations
    ATTN: OP 982, CAPT Toole
    ATTN: Code 604C3, Robert Piacesi
    ATTN: OP 982, LCDR Smith
    ATTN: OP 982, LTC Dubac

Chief of Naval Research
    ATTN: Technical Library

Officer-In-Charge
Civil Engineering Laboratory
Naval Construction Battalion Center
    ATTN: R. J. O'Dello
    ATTN: Technical Library

Commandant of the Marine Corps.
    ATTN: POM

Commanding General
Development Center
Fire Support Branch
    ATTN: CAPT Hartneady
    ATTN: LTC Gapenski

Commander
Naval Air Systems Command
Headquarters
    ATTN: F. Marquardt

Commanding Officer
Naval Explosive Ord. Disposal Fac.
    ATTN: Code 504, Jim Petrousky

Commander
Naval Facilities Engineering Command
    ATTN: Technical Library

Superintendent (Code 1424)
Naval Postgraduate School
    ATTN: Code 2124, Tech. Rpts. Librarian

Director
Naval REsearch Laboratory
    ATTN: Code 2600, Tech. Library

Commander
Naval Sea Systems Command
    ATTN: ORD-033
    ATTN: SEA-9931G

Officer-In-Charge
Naval Surface Weapons Center
    ATTN: M. Kleinerman
    ATTN: Code WX21, Tech. Library
    ATTN: Code WA501, Navy Nuc. Prgms. Off.

Commander
Naval Surface Weapons Center
Dahlgren Laboratory
    ATTN: Technical Library

Commander
Naval Weapons Center
    ATTN: Code 533, Tech. Library
    ATTN: Carl Austin

DEPARTMENT OF THE NAVY (Continued)

Commanding Officer
Naval Weapons Evaluation Facility
        ATTN: Technical Library

Director
Strategic Systems Project Office
        ATTN: NSP-43, Tech. Library

DEPARTMENT OF THE AIR FORCE

AF Armament Laboratory, AFSC
        ATTN: Masey Valentine
3 cy   John Collins, AFATL/DLYV

AF Institute of Technology, AU
        ATTN: Library, AFIT, Bldg. 640, Area B

AF Weapons Laboratory, AFSC
        ATTN: SUL

Headquarters
Air Force Systems Command
        ATTN: Technical Library

Assistant Secretary of the Air Force
Research and Development
Headquarters, U.S. Air Force
        ATTN: Col R. E. Steere

Deputy Chief of Staff
Research and Development
Headquarters, U.S. Air Force
        ATTN: Col J. L. Gilbert

Commander
Foreign Technology Division, AFSC
        ATTN: NICD, Library

Headquarters USAF/IN
        ATTN: INATA

Headquarters USAF/RD
        ATTN: RDPM

Oklahoma State University
Fld. Off. for Wpns. Effectiveness
        ATTN: Edward Jackett

Commander
Rome Air Development Center, AFSC
        ATTN: EMTLD, Doc. Library

SAMSO/RS
        ATTN: RSS

DEPARTMENT OF ENERGY

Division of Military Application
Department of Energy
        ATTN: Doc. Control for Test Office

Los Alamos Scientific Laboratory
        ATTN: Doc. Control for Reports Lib.
        ATTN: Doc. Control for Tom Dowler

DEPARTMENT OF ENERGY (Continued)

University of California
Lawrence Livermore Laboratory
        ATTN: Jerry Goudreau
        ATTN: Tech. Info. Dept., L-3
        ATTN: Mark Wilkins, L-504

Sandia Laboratories
Livermore Laboratory
        ATTN: Doc. Control for Tech. Library

Sandia Laboratories
        ATTN: Doc. Control for John Colp
        ATTN: Doc. Control for William Patterson
        ATTN: Doc. Control for John Keizur
        ATTN: Doc. Control for W. Altsmeirer
        ATTN: Doc. Control for Walter Herrmann
        ATTN: Doc. Control for 3141, Sandia Rpt. Coll.
        ATTN: Doc. Control for William Caudle

Department of Energy
        ATTN: Doc. Control for Tech. Library

Department of Energy
Division of Headquarters Services
        ATTN: Doc. Control for Class. Tech. Library

Department of Energy
Nevada Operations Office
        ATTN: Doc. Control for Tech. Lib.

OTHER GOVERNMENT AGENCIES

NASA
Ames Research Center
        ATTN: Robert W. Jackson

Office of Nuclear Reactor Regulation
Nuclear Regulatory Commission
        ATTN: Robert Heineman
        ATTN: Lawrence Shao

DEPARTMENT OF DEFENSE CONTRACTORS

Aerospace Corporation
        ATTN: Tech. Info. Services

Agbabian Associates
        ATTN: M. Agbabian

Applied Theory, Inc.
2 cy   ATTN: John G. Trulio

AVCO Research & Systems Group
        ATTN: Pat Grady
        ATTN: S. Skemp, J200
        ATTN: Research Library, A830, Rm. 7201
        ATTN: David Henderson

Battelle Memorial Institute
        ATTN: Technical Library

The BDM Corporation
        ATTN: Technical Library

DEPARTMENT OF DEFENSE CONTRACTORS (Continued)

The Boeing Company
       ATTN: Aerospace Library

California Research & Technology, Inc.
       ATTN: Technical Library
       ATTN: K. N. Kreyenhagen
       ATTN: M. H. Wagner
       ATTN: C. C. Fulton

Civil/Nuclear Systems Corp.
       ATTN: Robert Crawford

EG&G, Inc.
Albuquerque Division
       ATTN: Technical Library

Engineering Societies Library
       ATTN: Ann Mott

General Dynamics Corp.
Pomona Division
       ATTN: Keith Anderson

General Electric Company
Tempo-Center for Advanced Studies
       ATTN: DASIAC

Georgia Institute of Technology
Georgia Tech. Research Institute
       ATTN: S. V. Hanagud
       ATTN: L. W. Rehfield

Honeywell Incorporated
Defense Systems Division
       ATTN: T. N. Helvig

Institute for Defense Analyses
       ATTN: IDA Librarian, Ruth S. Smith

Kaman AviDyne
Division of Kaman Sciences Corp.
       ATTN: Technical Library
       ATTN: E. S. Criscione
       ATTN: Norman P. Hobbs

Kaman Sciences Corporation
       ATTN: Library

Lockheed Missiles & Space Co., Inc.
       ATTN: M. Culp
       ATTN: Technical Library

Lockheed Missiles and Space Co., Inc.
       ATTN: Tech. Info. Ctr., D/Coll.

Martin Marietta Aerospace
Orlando Division
       ATTN: M. Anthony
       ATTN: Al Cowen
       ATTN: H. McQuaig

Merritt CASES, Incorporated
       ATTN: Technical Library
       ATTN: J. L. Merritt

DEPARTMENT OF DEFENSE CONTRACTORS (Continued)

University of New Mexico
Dept. of Campus Security and Police
       ATTN: G. E. Triandafalidis

Newmark, Nathan M.
Consulting Engineering Services
University of Illinois
       ATTN: W. Hall
       ATTN: Nathan M. Newmark

Pacifica Technology
       ATTN: R. Bjork
       ATTN: G. Kent

Physics International Company
       ATTN: Doc. Control for Tech. Library
       ATTN: Doc. Control for Larry A. Behrmann
       ATTN: Doc. Control for Charles Godfrey
       ATTN: Doc. Control for Dennis Orphal

R & D Associates
       ATTN: Technical Library
       ATTN: Cyrus P. Knowles
       ATTN: Arlen Fields
       ATTN: Paul Rausch
       ATTN: William B. Wright, Jr.
       ATTN: Harold L. Brode
       ATTN: Henry Cooper
       ATTN: J. G. Lewis

The Rand Corporation
       ATTN: Technical Library

Science Applications, Inc.
       ATTN: Technical Library

SRI International
       ATTN: George R. Abrahamson
       ATTN: Jim Colton

Systems, Science and Software, Inc.
       ATTN: Edward Gaffney
       ATTN: Robert Sedgewick
       ATTN: Technical Library

Terra Tek, Inc.
       ATTN: Technical Library

TRW Defense & Space Sys. Group
       ATTN: Peter K. Dai, R1/2170
       ATTN: Tech. Info. Center/S-1930

TRW Defense & Space Sys. Group
San Bernardino Operations
       ATTN: E. Y. Wong, 527/712

Weidlinger Assoc. Consulting Engineers
       ATTN: Melvin L. Baron
       ATTN: J. M. McCormick

Weidlinger Assoc. Consulting Engineers
       ATTN: J. Isenberg